Antenna Characterisation and Optimal Sampling Constraints for Breast Microwave Imaging Systems with a Novel Wave Speed Propagation Algorithm.

by

Diego Rodriguez Herrera

A thesis submitted to the Faculty of Graduate Studies of

The University of Manitoba

In partial fulfillment of the requirements of the degree of

MASTER OF SCIENCE

Department of Physics and Astronomy

University of Manitoba

Winnipeg

Copyright © 2016 by Diego Rodriguez Herrera

Abstract

Breast microwave imaging (BMI) is a novel modality that complements current breast screening tools. Microwave radar imaging creates a radar cross-section (reflection) map of the breast. The difference in permittivity between healthy and malignant tissue is between 10-50%. This contrast is significantly higher than that obtained with x-rays and supports the use of microwave imaging for breast cancer diagnosis.

Prior to widespread clinical use, some areas require further study. Firstly, the performance of three different antennas was carried out, to assess their suitability for a BMI system. Secondly, the sampling constraint of a circular scan geometry was studied and tested using experimental phantoms and these antennas.

For accurate breast BMI reconstruction, the transmission speed of the radio waves inside the breast must be determined. The tissue composition of each patient is different, making this task challenging. This work presents an algorithm for wave speed estimation in different mediums.

Contributions

This work, like most contemporary scientific research, was done in an interdisciplinary work environment where there was collaboration with the various members of the group. However, it is important to define the work that was done by the author to better place this thesis in context.

This work contributes to the microwave imaging field, with an emphasis on filling the gap between theoretical knowledge and experimental results. To this end, the characterisation of four microwave antennas was performed. A framework based on image quality metrics was developed to compare the results between different antenna configurations.

A theoretical approximation is presented for the number of scan locations needed in a microwave imaging scenario with a circular path. The mathematical theory was presented in previous work, but the contribution of the present research focuses on the experimental testing of this theory.

The current thesis proposes a novel speed-search algorithm based on independent and objective image quality metrics. While this approach has been used in other imaging applications, its use in breast radar systems has, to the best of our knowledge, not previously been experimentally validated. A series of practical considerations are presented to allow for a more reliable speed search.

The datasets generated using Vivaldi and custom horn antennas were obtained from a group effort, and the data collected using the commercial horn antennas were generated by the author.

The author was also responsible for the image quality analysis presented here, and the Matlab code used to perform the analysis. The reconstruction algorithm has been published previously, but the author created a series of filters to improve the final image as described in chapter 4.

Acknowledgments

I would like to thank Dr. Stephen Pistorius for the guidance provided during this work. He constantly provided encouragement to explore new angles in research. Thanks to the opportunities he had facilitated I have grown as a researcher and as a person. I would also like to recognize the help provided by other members of the group. Dr. Daniel Flores for providing a close guidance during my degree, and always sharing his knowledge eagerly. Mario Solis for the help provided to design experiments and the lab work required for this thesis.

I am also grateful to my thesis committee Dr. Jason Fiege, and Dr. Sherif Sherif for the comments on my work and for providing guidance.

I would like to thank the support staff at the Department of Physics and Astronomy for supplying the resources needed for my work.

Last but not least I would like to thank Research Manitoba for the funding provided during this work.

Dedication

To my parents Juan Lauro and Maria Refugio for their patience and support, and the encouragement to achieve my dreams. And to Cyndi, who provided me with a renewed motivation to achieve my goals.

Table of contents

List of tables

List of figures

1 Introduction to microwave imaging for breast cancer detection. Review of current systems used in volunteer trials.

1.1 Background and justification

In 2015, an estimated 25,000 Canadian women were diagnosed with breast cancer and 5,000 of those women may die as a result [1]. Early diagnosis of breast cancer is vital to increase the survival rate of patients. The most commonly used method for detection is X-ray based mammography. The limitations of mammography are that it uses ionizing radiation, it is uncomfortable for the patients, and the false positive rates range from 60% to 70% [3]. Ionizing radiation places a limit on the number of repeated screenings that can be performed in a given time frame due to the effects of cumulative exposure to radiation. Research is focused on developing technologies that may overcome these limitations without too much compromise in sensitivity or cost [3].

Microwave imagining is a promising technology being studied for breast cancer detection. This system works by sending pulse-like signals from antennas placed around the breast and then recording the echo. Microwave technology has the advantage of being non-ionising and thus allowing for more frequent and earlier scans [2].

When compared to other non-ionising techniques, like Magnetic Resonance Imaging (MRI) or Ultrasound (US), Microwave technologies have some key advantages. While MRI offers a high-resolution image, the size and cost of MRI make it impractical as a screening tool. Ultrasound technologies may be less expensive than MRI, but the outcome is operator dependent yielding a high number of false positives. In mass production, microwave technologies have the advantage of being inexpensive and compact, making it easy to transport to remote locations. Due to the high

contrast between malignant and healthy tissues, breast microwave imaging (BMI) offers a viable alternative that may yield fewer false positive results. [2]

Microwaves may be generated and recorded using a Vector Network Analyser (VNA). A VNA is a piece of equipment that allows for analysis of circuits (also known as networks). This equipment allows for a high precision analysis that shows the response of the network in a very detailed manner.

A radar system can be comprised of a VNA paired with an antenna [4]. A VNA can generate signals with a flat response, with high precision, in the frequency domain. This flat response changes once the radio frequency (RF) signals are transmitted through an antenna. These are known as the reflection coefficients and determine the bandwidth of the antenna. The bandwidth of the antenna is the frequency range in which the antenna performs under the desired parameters for the current application. [4]

Microwave radar systems create a reflectivity map that helps detect malignant lesions. The quality of the obtained image is dependent on the algorithm and parameters used for reconstruction. The propagation speed is one of the reconstructions parameters that have an impact on image quality.

1.2 Microwave imaging for breast cancer detection

Microwaves have been used for detection or tracking since the early part of the 20th century when radar systems were in development across the world for military purposes. Later, this technology expanded to other areas, for example, weather monitoring and prediction, air traffic control, underground surveys, and sea floor exploration amongst others. [6]

The use of microwave imaging in the medical field has been limited. While MRI systems have a radio frequency component, standalone microwave imaging devices were rare. In the last 25 years, the interest in MI has increased. Different groups have developed and tried microwave imaging systems, going as far as starting early clinical trials.

Microwave imaging is a promising technology that presents a series of challenges. One of the first challenges comes from skin reflection of RF signals. This is due to the significant difference in relative permittivity (ε_r) between air and living tissue. This work considers only the real part of the relative permittivity (ε_r), and the conductivity (σ). Skin has a ε_r of 30 whereas air is close to 1 (depending mostly on ambient humidity). Using a matching liquid mitigates the reflections from the skin, making it easier for the radio wave to penetrate the breast. Different groups have used a variety of substances as a coupling medium to limit the loss with the skin interface. However, using a liquid may present other problems, such as a loss of power, since these coupling materials have a high loss factor. Another issue is the insulation of connectors and antennas to avoid any mismatch in the feed line to the antenna. [7]

Tissue inside the breast, like fat or muscle, will cause additional losses of RF power due to reflection and dissipation. After the skin barrier, the RF signal also experiences a loss of power in the different tissues inside the body. A 10 GHz signal would experience more than 80 dB in attenuation after several centimeters traveling inside the body. The attenuation places a constraint on what type of imaging can be done using microwaves. For this reason, imaging of deep body tumors (e.g. liver or kidney) may not be viable with current technology. Breast tumors are closer to the skin and may not require more than 10 cm of penetration to detect an abnormality.

Other medical uses for microwave imaging include detecting brain injury types [9] or monitoring urine volume in the bladder [10]. These applications are still in early phase of research. As the technology becomes more mature, new applications may emerge.

Microwave imaging creates a reflectivity map that shows the conductivity and permittivity as a function of position inside the breast. Permittivity is mostly related to the water content in the tissue, while conductivity is affected primarily by the presence of ionizing molecules, like salt. The contrasts between malignant and healthy tissues give microwave imaging its greatest advantage. In BMI systems the ratio between the permittivity of the malignant tissue and the permittivity of healthy tissue is known as the contrast.

Measuring the dielectric properties of living tissue is a challenge. Doing measurements in vivo requires an invasive surgical procedure and poses a risk to the patient. If the tissue properties are measured after it is extracted from the body, the properties may change the longer the tissue is outside the body. This is because dielectric measurements depend on water content and tissues removed from the body dehydrate. Early studies showed that the contrast may be higher than a factor of 10. New studies have shown that this applies only to fatty tissue while the contrast with fibroglandular tissue may be lower. One recent 35 patient study from Sugitani et al. shows a difference of a factor of 6 between tumors and fatty tissue at 1GHz and a contrast of 1.5 for fibroglandular tissue. The contrast value decreases for higher frequencies. For comparison x-ray mammography works with contrasts as low as 4-10% [7, 11].

The penetration of the radio waves inside the tissue is affected by a phenomenon known as the skin effect. The small currents caused by the application of an EM field to any material attenuate the signal power inside the material. In conductors, the current generated by an EM field would be high

thus the depth penetration of the field would be low. While human tissue is a poor conductor, this phenomenon is still present. A good approximation of the radio wave penetration is shown in equation (1.1)

$$\delta = \left(\frac{1}{\omega}\right)\sqrt{\left(\frac{\mu\varepsilon}{2}\right)\left[\left(1+\frac{\sigma^2}{(\omega\varepsilon)^2}\right)^{1/2}-1\right]}\ \text{m}, \tag{1.1}$$

where δ is known as the skin depth parameter and is equal to the distance on the material where the field falls to e^{-1} of the value it had at the interface. μ is the relative permeability. ε is the permittivity of the material and σ is the conductivity. At depth 5δ the power falls by 40dB, and the amplitude of the field is only 1% of that at the surface. [8]

The performance of microwave systems used for breast cancer detection depends strongly on the range of frequencies used. Equation 1.1 shows that higher frequencies have less penetration, and while this may imply that low frequencies are optimal for microwave imaging, it is important to note that resolution is also tied to frequency because of the diffraction limit. A good estimation of resolution is about ¼ wavelength of the maximum frequency. These opposing trends, mean that at a 3 cm depth the power of a 900 MHz signal, with a maximum resolution of approximately 4 cm, falls to 1% of that at the surface (with an average propagation speed of 1.5 $x10^8$ m/s inside the body).

The selection of the frequency range used in microwave imaging should be a balance between these two opposing objectives. JC Lin [12] has shown that the ideal frequency range should be between 2 and 8GHz when accounting for resolution and attenuation inside the body. In more recent years, new reconstruction techniques have emerged that take advantage of near-field

measurements, where information that is not affected by the diffraction limit can be measured. [12, 7]

1.3 Current state of microwave technology

There are a number of groups around the world in different stages of research, working on microwave imaging for breast cancer detection. At the University of Manitoba, there are two groups using microwave imaging technology. One led by Dr. LoVetri in the Engineering Department, and the other one led by Dr. Pistorius in the Physics Department. Both groups collaborate and an initial safety trial was carried out in the last quarter of 2015. There are plans for a phase one clinical trial.

In this section, a review of four current systems is given. First an overview of three systems by groups who have presented volunteer or patient results, and then an examination of the system developed in the Physics Department at the University of Manitoba. [7]

1.3.1 Dartmouth College system

The Dartmouth College uses microwave tomography for clinical breast imaging. The system has been in use for a number of years. In this review, we describe the third iteration of this system. [13]

1.3.1.1 Hardware Design

The current system uses an Agilent ESG-D series 4432B as the RF signal generator. The output is fed into a power divider network that allows for 16 channels of coherent reference signals.

A series of switches allows the 16 channels of the system to be used as receivers or transmitters. In this case, while one single channel is transmitting the others are in receiving mode to sense reflections from the object being scanned. The system operates in the range of 0.5 GHz to 3 GHz.

The 16 channels are connected to a monopole antenna array. To limit the scatter at the breast boundary, the antennas are housed in a chamber filled with a mixture of water and glycerine as a coupling medium. [13]

In air, monopole antennas have a narrow bandwidth, but when used in a coupling medium the bandwidth broadens due to resistive loading. This system has return losses above 10 dB in the operating frequency range. As a result of the coupling medium, the skin reflection is minimized.

The monopole antenna is made of coaxial cable of 2.3 mm in diameter. A protective polyoxymethylene sleeve of 3.4 cm covers the top of the antenna. A 4.4 mm diameter stainless steel rod covers the rest of the feedline. This arrangement allows for a rigid antenna that slides through hydraulic seals in the tank base during antenna motion. This configuration allows for flexible positioning of the antennas.

Data capture in the system is done in two distinct modes, 2D, and 3D. For a 2D mode, the 16 antennas move as a single array unit. Every antenna acts as a transmitter while the rest (15 antennas) are in receiver mode. This procedure is repeated for every antenna, generating 240 measurements for every frequency. The antennas are moved down in 7 different planes for data collection. The plane separation is dependent on breast size.

The 3D mode uses two arrays of eight antennas to allow for cross plane measurement. For each measurement, the antennas in array 1 (A1) stay in the same plane while the antennas in the second array (A2) move down to the next plane. Once the antennas in A2 reach plane 7, they move to the first plane and the antennas in A1 move to the second plane, repeating the same pattern. This yields 49 positions for the different antennas arrays when 7 planes are used. [13]

The system uses a gain calibration setting, where every antenna starts with a 1x gain and the gain is adjusted until there is parity in all the receiving antennas. An additional calibration is performed to account for the cable length of the antennas (to removes phase errors) and to diminish the three-dimensional propagation losses. This method requires measurement of the homogenous background (glycerine-water mixture) and a second measurement with a target. [14]

1.3.1.2 Reconstruction

After the system takes all the measurements of the breast, a reconstruction using a finite-difference-time-domain (FDTD) algorithm is carried out. FDTD is used to reconstruct the dielectric properties (permittivity and conductivity) of the breast by solving Maxwell's equations in an iterative fashion. This reconstruction technique employs near-field measurements and has the advantage of not being affected by the diffraction limit. However, FDTD can be slow to compute, especially when 3D models are reconstructed. In addition, FDTD models may have trouble with odd shaped targets, for example, the nipple. [7 15]

1.3.2 University of Calgary system

In 2013, the University of Calgary presented results of a patient study from a microwave imaging system. The radar technique they use is known as TSAR (tissue sensing adaptive radar). The system uses a monostatic configuration requiring only one antenna. [15]

1.3.2.1 Hardware design

The system employed by the Calgary group consists of a padded bed over a tank that is filled with canola oil as a coupling medium. The system uses a custom Vivaldi antenna with a director (BAVA-D) with a bandwidth of 2.4 GHz to 18GHz. The antenna is attached to an arm that allows for vertical movement over a span of 24 mm to 141 mm below the lid of the tank. To rotate the antenna

around the breast, the full tank rotates, allowing a cylindrical scan geometry. A laser sensor is attached to the arm, to allow for an outline reconstruction of the breast.

The antenna is connected to a vector network analyzer (VNA) from Agilent (8722ES). A 3 m long cable is used to connect the antenna to the VNA, and a cable guiding system allows for repeatability when the antenna moves. The system is calibrated at the end of the cable in the same feed the antenna is plugged in. The VNA takes 1601 points, from 50 MHz to 15 GHz, with a power of -5 dBm. The TSAR prototype can scan a breast with 200 positions in under 30 minutes.

The system has a camera mounted on the side of the tank. The camera allows for visual feedback of the position of the antenna and helps to plan the scan locations around the breast. A scan of the empty tank is done to generate a reference signal that is subtracted from the patient scan. Two different metallic targets are also scanned to confirm the dielectric constant of the medium and to measure the delay in distance relative to the end of the antenna. [17]

1.3.2.2 Reconstruction

The algorithm takes calibrated data and uses a neighborhood-based approach to estimate the skin reflection. The laser information is used to assess a ROI (Region of interest). The algorithm focuses on this ROI. For each scan location, the data is squared and the travel time to the ROI is estimated, as shown in (1.2)

$$I(X) = \left[\sum_{n=1}^{N} s_n\left(\tau_n(x)\right)\right]^2, \tag{1.2}$$

where τ_n (x) is the estimated travel time to the focal point x, s_n (t) is the value of the signal at position n. For this algorithm, an ε_r of 9 is used to estimate travel times. This is repeated for every scan location and summed to provide a final image [16]. In more recent publications, the Calgary

group has used a combined approach based on radar and tomography reconstruction. First, a radar algorithm is used to create a rough outline of the target. This information is then fed to the start point for a finite element contrast source inversion (FEM-CSI) algorithm. This allows for higher resolution images that resolve more details. [18]

1.3.3 University of Bristol system

The University of Bristol has developed a system made of an antenna array arranged in a semi-spherical fashion. This system is an ultra-wide band radar system (UWB).

1.3.3.1 Hardware design

The antenna array is made of small patch antennas with a cavity in the back to shield the antenna from interference. The bandwidth of the antenna is between 4 and 9 GHz. Different iterations of this system were built. The first semi-spherical system used 24 antennas while the later versions used 60 antennas.

A multistatic approach with a high number of antennas has some advantages. One of them is that the scans can be done very fast since there are no moving parts (around 10 seconds in the last prototype). A high amount of information is collected and, in theory, this would improve the image quality. On the other hand, having a large number of antennas presents some challenges. The cross talk between antennas can cause interference in the measurements. For this reason, the antennas need to have a cavity in the back for shielding along with radar absorbent material (RAM) between the antennas. Most VNAs have a limited amount of ports (between 1 and 10), so a high-speed switch is needed to perform measurements with all antennas. Careful consideration is required for the arrangement of antennas since there is a small clearance for cables. [19]

1.3.3.2 Reconstruction

The Bristol group uses a confocal data-adaptive algorithm. This algorithm weights and time-shifts every scan waveform based on an average speed and attenuation in the medium, and is repeated for every voxel. This weighting changes with the distance of said voxel to every sensor. The algorithm processes every waveform iteratively until each voxel is in the correct position. [7,4 19]

1.3.4 University of Manitoba system

One of the systems being developed at University of Manitoba is based on a radar approach. This system has been through a few revisions. In this section, we describe the hardware of the first iteration of the system and the reconstruction algorithm that forms the basis for the work of this thesis. In later chapters, a more detailed description is presented with new revisions to the system.

1.3.4.1 Hardware design

The first experimental system consisted of a 56 x 56 x 40 cm^3 tank made of Plexiglas. A Vivaldi antenna was used for a monostatic reconstruction. Canola oil was used to provide a coupling medium between the antenna and a breast phantom. An Anritsu MS2026A VNA is used to generate and record the signals.

The Vivaldi antenna is manufactured using two layers of Arlon-Diclad 527 and has a bandwidth in air of 3.3 GHz to 10 GHz. The antenna is encased in a sealed acrylic structure to avoid oil from entering the connection feed of the antenna. If oil is present in the connection feed, there would be mismatch impedance that would cause the antenna to behave erratically.

The breast phantom was made using a styrene-acrylonitrile cylinder with a diameter of 13 cm and a height of 35 cm. A skin layer was simulated with a mixture of corn syrup and agar gel.

Glycerin was used in place of breast tissue while an 85% saline and 15% fructose solution served as synthetic tumors in a spherical container. Fibroglandular tissue structures were created with a mixture of 50% wheat flour and 50% saline.

This first system was used as a proof of concept. Since then, significant improvements have been made. A current description of the system can be found in chapter 2. [20]

1.3.4.2 Circular holography algorithm

The reconstruction algorithm being used is a technique known as microwave holography, where most of the processing is carried out in the frequency domain. The data collected is fed into the algorithm in the time and angular domain. Each angle corresponds to the position of the antenna around the scan location. A two-dimensional Fourier transform is done to manipulate the data in the frequency domain. A matched filter (shown in 1.3) is used to compensate for the circular scan trajectory.

$$e^{-j\left(\sqrt{4k^2R^2-\varphi^2}+\varphi\sin^{-1}\left(\frac{\varphi}{2kR}\right)+\varphi\pi\right)}. \quad (1.3)$$

The variables for the matched filter are $k = \omega/c_n$ known as the wave number, R as radius of the scan geometry, and ϕ as the angular spatial frequency domain.

Afterwards, a mapping is needed to transform data from the time and angular domain to a spatial domain; finally, an interpolation is applied to allow the use of the inverse Fourier transform. The algorithm is summarized in figure 1.1. [21]

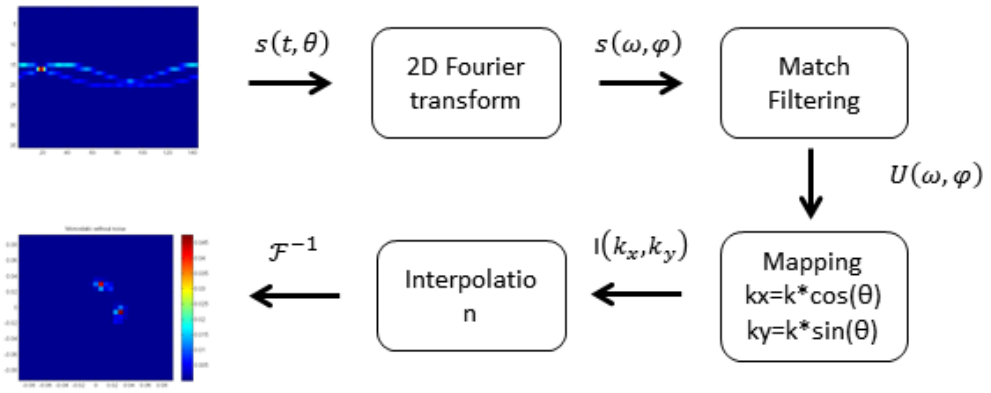

Figure 1-1 Summary of microwave holography algorithm. From the raw data to the reconstructed image. The raw data is recorded in a matrix where the rows represent the time domain, and the columns are the angular position of the antenna. A 2D Fourier transform is performed. Then the matched filter is applied to compensate for the scan trajectory, a mapping is done, and an interpolation takes place to compensate from uneven sampling due to the circular scan path.

1.4 Objectives of this study

The work presented in this thesis is a continuation of the work done in Dr. Pistorius laboratory. Currently, the microwave imaging system being developed at the University of Manitoba has just finished a volunteer safety trial and a phase one clinical trial is scheduled for this year.

Section 1.3.4 describes an early experimental set up of the system used at the University of Manitoba. In the benchtop system, the scanning chamber consists of a Plexiglas tank, where the antennas were stationary, and the phantom was rotated. Initially, the phantoms were cylindrical, and the scans were performed in a single plane. This arrangement proved useful to demonstrate the capabilities of a radar system, but a more complex system was needed to scan human subjects.

To image human subjects, there are a number of challenges to be addressed. The mechanics of the new system were designed by Mario Solis, a member of the Dr. Pistorius group. The design consists of a bed on which the patient lies in a prone position and where an aperture at the chest level allows for the breast to enter the scan chamber. The scan chamber is surrounded with radar

absorbent material. A rotary table moves the antennas along with the VNA and power supply. A second motor allows the height of the antennas to be changed to scan different regions of the breast.

With a new mechanical design, the VNA and antennas used in the system had to be changed. The impact of the changes to using air as a coupling medium instead of oil needed to be investigated. This change also resulted in the need to characterize new antennas, since the Vivaldi antennas of the first system were designed to work in oil.

Performing scans with patients brings new constraints. When performing experiments on phantoms, it takes up to one hour before the dielectric properties of the phantom change. With a patient, the scan has to be performed quickly, to avoid any physical change of position and breast shape. In addition, other factors which need to be considered are patient comfort, and breast immobilization. One way to reduce the examination time is to use fewer scan positions.

The reconstruction algorithm requires an estimation of the propagation speed of the wave inside the breast. When performing experiments in phantoms the dielectric properties of the phantom are known, so an approximation for the propagation speed can be made. This approximation is challenging when scanning patients since each breast has a different tissue composition and shape.

Developing a BMI system with the capability to scan volunteers was a team effort performed by various members of the non-ionizing imaging lab. This thesis documents the problems investigated and innovative solutions that the author has implemented.

Chapter 2 presents a comparison of four different antennas and highlights the differences between custom made antennas and commercial antennas. This comparison drove the decision to use the commercial horn antenna in the clinical system.

In Chapter 3, the results of a sampling constraint study are presented. The clinical system is controlled by a set of motors. The delay in the motor movement and scan time means there is a trade-off between the number of scan locations and the time it takes to do a scan. This study aims to find the minimum number of scan locations needed to generate a useful image. The results of this chapter show that it is possible to reduce the scan time of a patient, while still generating useful data.

In Chapter 4, a study to estimate the wave propagation speed is presented. Microwave holography image formation techniques require an estimate of the propagation speed in the medium [21]. Since this imaging technique creates a reflectivity map of the breast region by processing time delays between the irradiated wave and the recorded breast structure responses and converting those delays into distances, this parameter is crucial to forming accurate images. If an erroneous propagation speed estimate is used, the phase information will migrate the breast structure responses to erroneous spatial locations, reducing the probability of tumor detection and creating artifacts in the image. To obtain an optimal estimate, auto-focus techniques are used. These methods yield a propagation speed assessment by performing an optimization process in which image quality metrics are used as the cost function. In Chapter 4, a comparison of different image quality metrics is presented. Simulated and experimental datasets are used to evaluate the fitness of these image quality metrics.

2 Hardware characteristics and considerations of the BMI system.

2.1 General description of BMI systems

The features of the UM breast microwave imaging (BMI) system being used have been updated during the previous four years. While most components have changed the general configuration of the technology remains similar.

The system is controlled by a PC that runs a custom-made program. The software was first prototyped in LabVIEW and later coded in C#. The computer communicates with a set of motors. In the first iteration of the system, the motors moved the phantom to simulate a circular scan geometry. The more recent version of the system rotates the antennas to allow for the scanning of human volunteers. The PC also communicates with a VNA for the collection of the microwave signals. The program ensures that the movement of the motors and the measurements of the VNA are synchronized.

This chapter describes the characteristics of the hardware used in the BMI system. It also presents the study performed to select a set of antennas that will work in a clinical system. Section 2.2 is an introduction to VNA calibration. The characteristics of the antennas and a comparison are presented in section 2.3. In section 2.4 a detailed description of the VNAs used in the system is given, along with a comparison between them.

2.2 VNA Calibration and special considerations

In any measurement, there are uncertainties, which are manifested as a deviation of the measurement when compared with the true value. There are two types of uncertainties. Type A uncertainties are random measurement errors that cannot be systematically corrected. These

errors can be statistically modeled. Type B uncertainties are reproducible and are systematic. These errors can be corrected.

While type A uncertainties are not systematic, some of them can be avoided. Thermal drift is a type A uncertainty that occurs when the device suffers a temperature change. Materials change dielectric properties when there is temperature change. Thermal drift would alter the performance of the system over a time period. To achieve thermal equilibrium a warm up period for VNAs is recommended before using them. As part of our calibration procedure a half hour warm-up period for the VNA was observed.

When connecting the VNA to the antennas the cable used introduces a phase delay. The delay is dependent on the frequency used and cable length. Some high-quality cables present a constant delay over a frequency range. The phase delay $\tau_p(f)$ can be calculated with equation 2.1, where f_{stop} and f_{start} are the selected frequencies for the sweep range. [4]

$$\tau_p(f) = -\frac{arg\left(s_{21}(f_{stop})\right) - arg(s_{21}(f_{start}))}{360°(f_{stop} - f_{start})} \quad (2.1)$$

The phase at 0Hz is assumed to be 0, so $\arg\left(s_{21}(0Hz)\right) = 0$. s_{21} is the measurement read in port 2 from port 1. Figure 2-1 shows the different S-parameters and their meaning.

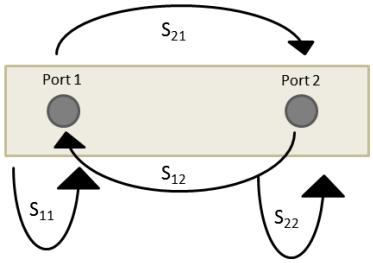

Figure 2-1 S-parameters for a two-port VNA, when sending a signal from Port 1 to port 2 it is known as S_{21}, S_{11} and S_{22} refer to measurements done with open ports where there is a reflection of the wave at the termination point.

Once the phase delay is known the electrical length (l_{el}) can be calculated for the transition line using the speed of light and the phase delay, as shown in equation 2.2,

$$l_{el} = c_0 \tau_p \tag{2.2}$$

It is also possible to calculate the phase delay τ_p of a homogenous transmission line if the relative permittivity ε_r, is known.

$$\tau_p = \frac{l_{mechanical}\sqrt{\varepsilon_r}}{c_0}, \tag{2.3}$$

a calibration kit is used at least daily to ensure that our measurements did not suffer from systematic errors. The calibration was performed over the range of frequencies being used. For our system, short, open and matched loads were used for calibration, along with an S_{12} and S_{21} measurements. The "unknown through" option is used during calibration to eliminate the phase delay caused by the length of the cables being used. The unknown through option can only be used if the condition S_{12}= S_{21} is met. [4]

2.3 Antennas description, characterization, and comparison

2.3.1 General antenna characteristics

The characteristics of the radar system are closely tied to the type of antenna used. The resolution, angular resolution, bandwidth and sensitivity are all linked to the type of antenna in the system. The antenna works in combination with other parts of the system to meet the specifications needed. For example, an antenna with a high bandwidth needs to be driven by a VNA that matches the bandwidth.

The range resolution of the system is tied to the bandwidth. A radar system transmits a pulse with a duration of τ seconds. When the radar receives a reflection at time t_0 then the object (1) is at a point of $x_1 = ct_0/2$. The reflected signal can overlap with a second object (2) that is at a distance of $c\tau/2$ from object 1. If object 2 is at $x_2 = c(t_0 - \tau)/2$, then the system has no way to discriminate between the two. The expression $c\tau/2$ defines the range resolution of our radar system (Δx). We can relate this resolution range to the frequency domain. A Fourier transform of a rectangular pulse is a sinc function with a main lobe width that is inversely related to the rectangular pulse duration. An approximation of $\tau \approx 1/B$ can be used, where B is the bandwidth of the system. Equation 2.1 makes use of the approximations described to generate a range resolution equation. [6, 29]

$$\Delta x = \frac{c\tau}{2} = \frac{c}{2B}. \tag{2.4}$$

The sensitivity of an antenna is related to the gain of the antenna. The gain is dependent on the radiation pattern, and normally the maximum gain is quoted. The gain is defined as the ratio of the intensity of the antenna when compared to an isotropic antenna.

Four different antennas were tested in the imaging system presented. The system uses a broadband antenna to increase the range resolution. A beamwidth that covers only the ROI is also desirable, to help diminish power loss. The current section would focus on discussing the strengths and disadvantages of each antenna type tested. A Fieldfox N9923A VNA is used to test all the antennas. The commercial horn antennas have a bandwidth of 2 to 20 GHz, while the maximum bandwidth of the Fieldfox is 6 GHz. A second test with a Copper Maintain VNA was performed to test the commercial horn antennas to a bandwidth of up to 8 GHz.

2.3.2 Vivaldi Antennas

Vivaldi antennas are made of a dielectric and a conductor subtract printed on both sides. The first version of the system used a double layer Vivaldi antenna (DLVA), made of two dielectric plates. Vivaldi antennas have a high gain, 7dBi on average. DLVA are broadband allowing for a better resolution.

DLVAs present a very useful radiation pattern, with a wide beam in the H-plane and a narrow beam in the E-plane. The narrow beam allows the system to create 2D slices of the 3D ROI. Creating a 2D reconstruction slice is faster than a more complex and slower 3D reconstruction. [22]

The antenna used in the system has Arlon-Diclad 527 as substrate with a relative permittivity of ε_r =2.4-2.65. The thickness of the substrate is 0.00625 inches. The antenna is designed to operate in the 1 GHz to 6 GHz range (Figure 2-2 shows a 0.74 GHz to 6+ GHz -5 dB bandwidth). The antenna is attached to a special acrylic housing to allow the antenna to be submerged in canola oil. The acrylic has similar dielectric properties as the dielectric used in the antenna. [20]

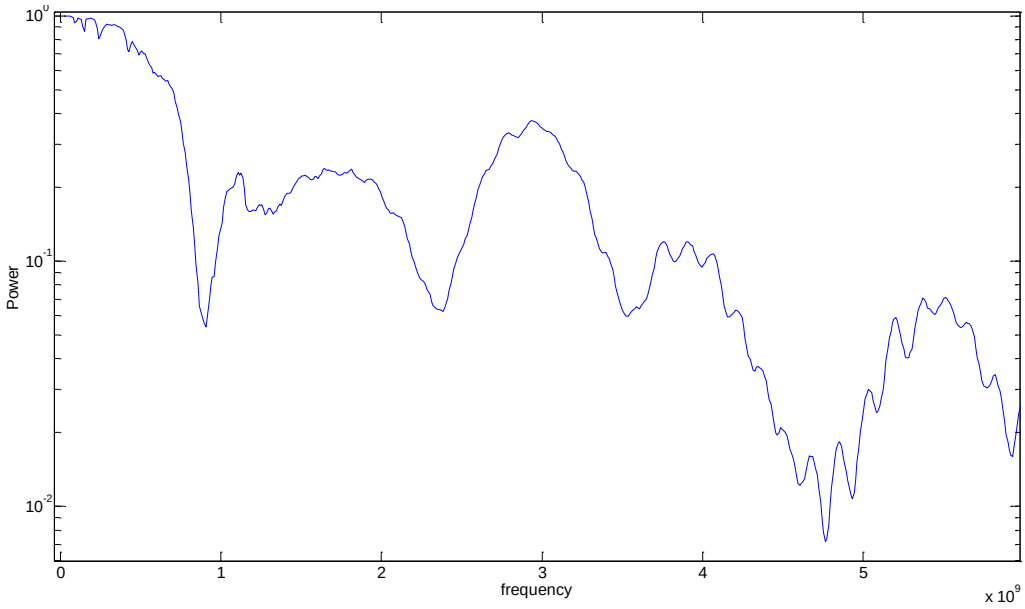

Figure 2-2 S11 response from Vivaldi antenna. With a -5 dB bandwidth of 0.74 GHz to 6+ GHz.

2.3.2.1 Vivaldi antennas phase delay

Cables and antennas introduce a phase delay to the signal generated by the VNA. As mention in section 2.2 the phase delay introduced by the cable can be eliminated using a calibration kit and an unknown through setting. Phase delay calibration is more complicated for the antennas that were used since no calibration kit was designed for these antennas. An experimental measurement was made to account for the phase delay.

To measure the phase delay of the antenna a measurement of a highly reflective metallic plate of 0.1 m by 0.2 m was used as a target. The plate was positioned at 0.01 m from the edge of the antenna, and the moved in 0.01 m increments. 20 measurements were taken. Once the data were collected, the position of the plate was obtained by using the signal to determine the location of the peak response and the full-width at half-maximum. A linear regression was performed to estimate the phase delay of the antenna.

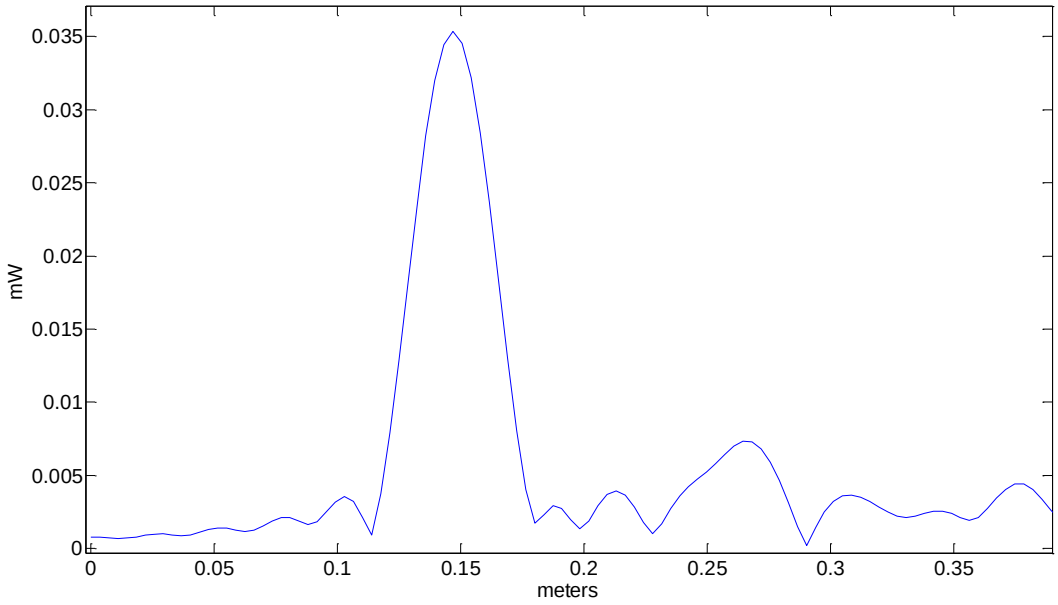

Figure 2-3 Time domain reflection from the metallic plate at 0.01 m from the edge of a Vivaldi antenna. The maximum peak is at 0.147 m, and the lobe has a full-width at half-maximum (FWHM) of 0.037 m.

Using the 20 measurements taken a linear regression was performed. The data was fitted to equation 2.4, where y is the distance obtained in the VNA sweep. X is the measured distance from the edge of the antenna to the target. The results were $p_1 = 1.009$ (slope) and $p_2 = 0.1392$ (intercept). The slope of 1 is expected as there is a 1:1 relation from the movement of the target and the return signal. The intercept of p_2 tell us that the antenna has a phase delay equivalent to 0.1392 m. The regression has an R-squared of 0.9996. Figure *2-4* shows the data used for fitting.

$$y = p_1 x + p_2 \tag{2.5}$$

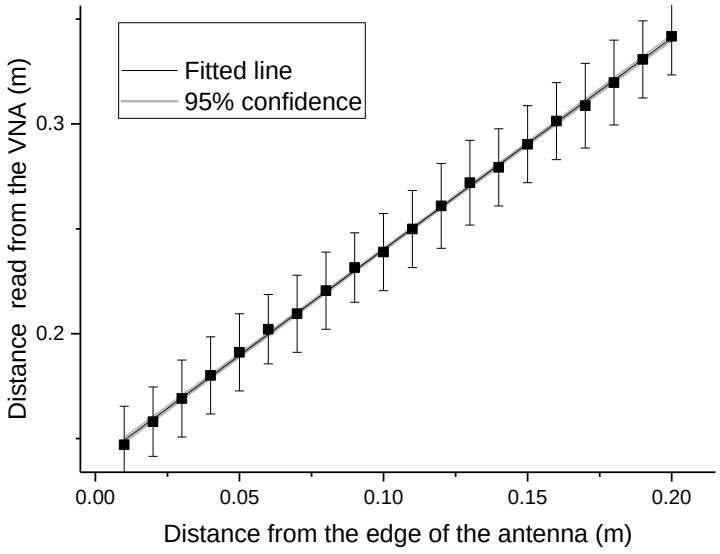

Figure 2-4 Data used for linear fitting to find the phase delay of the Vivaldi antenna. The error bars show the half-width of each of the measurements done; all the curves follow a similar pattern as Figure 2-3. The fitted line has the values $p_1 = 1.009$ *and a* $p_2 = 0.1392$

2.3.3 Planar Elliptical Monopole antenna.

A small elliptical monopole antenna was tested for the MIS. The advantage of this antenna type is that they are very small in size, and would allow for a smaller system. With smaller size antennas there is also the possibility of using a higher number of antennas for testing. The trade-off comes in the form of lower gain and a reduced bandwidth when compared to larger ultrawide antennas like Vivaldi or Horn antennas.

The antenna uses an elliptical design. Square antennas have better pattern stability while circular antennas have a wider bandwidth. The elliptical design is a compromise between the two. The substrate of the antenna has a ε_r = 9.8 and a thickness of 1.58 mm. The antenna is designed to work submerged in glycerin as a coupling medium and works in the 1 GHz to 4 GHz frequency range. [24]

Due to poor performance and time constraints, the planar antenna phase delay test was never performed. The planar antenna was designed to work in glycerin. However, due to high loss from

glycerin, the antennas did not record a usable signal. A second test was performed using oil as a matching medium. This second test produced a usable signal, but when reconstructed there were target misplacements and artifacts. The elliptical antennas were not used due the bad performance described.

2.3.4 Custom-Made Horn Antennas

A double-ridged horn antenna was designed to be submerged in oil as a coupling medium. The antenna was designed to operate at 1.5 GHz to 5 GHz range when submerged in oil (Figure 2-5 shows a bandwidth of 1.8 to 6+ GHz a change of 0.3 GHz from the design). The antenna is made of brass. Horn antennas have a high directivity and are broadband by nature. Horn antennas have a direct correlation between frequency and size. The lower the minimum operating frequency, the bigger the size of the antenna. [23]

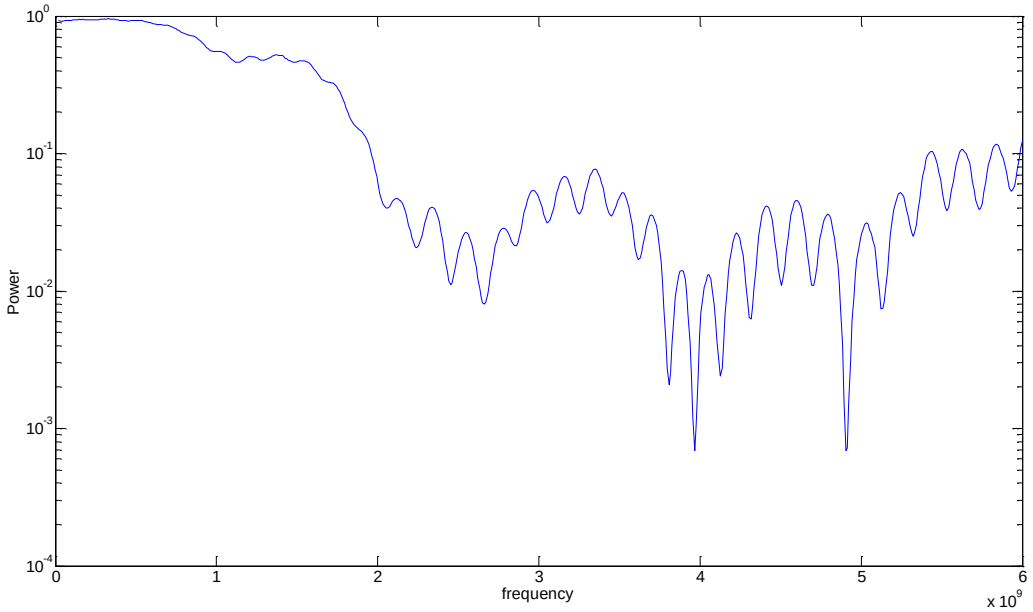

Figure 2-5 S11 response from custom horn antenna with a -5 dB bandwidth of 1.8 to 6+ GHz when submerged in oil. The antenna was designed to operate from 1.5 to 6 GHz. This is one of the inconsistencies introduced by the manufacturing process.

2.3.4.1 Custom-Made Horn Phase delay

To measure the phase delay of the horn antennas an experiment similar to the one described in 2.3.2.1 was carried on. Figure 2-6 shows the first reflection from a metallic plate at 0.01 m from the edge of the antenna. The main lobe of the custom horn antenna is wider than for the Vivaldi antenna.

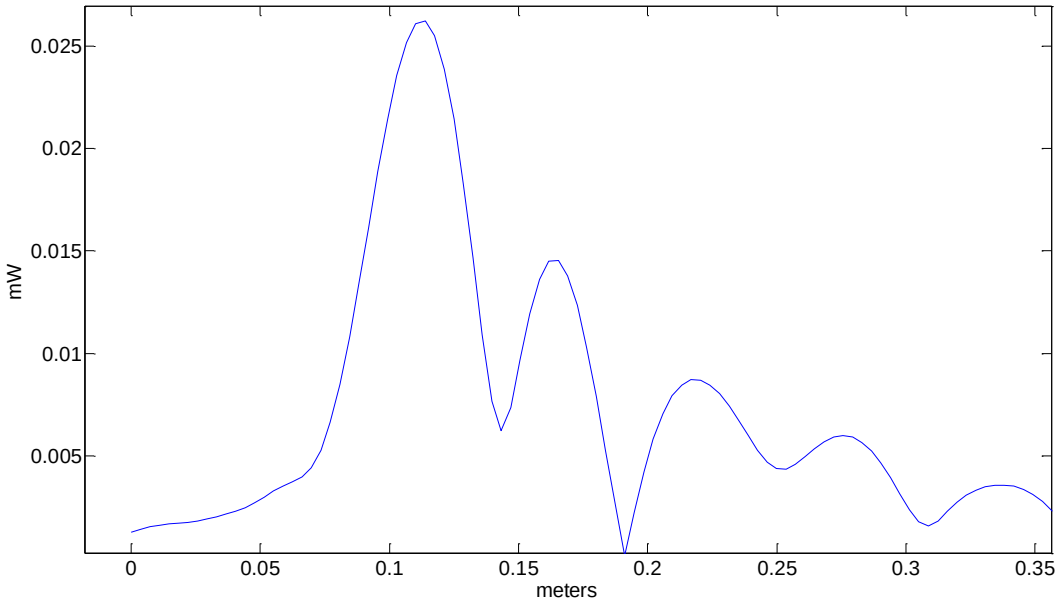

Figure 2-6 Time domain reflection from the metallic plate at 0.01 m from the edge of a custom horn antenna. The maximum peak is at 0.107 m, and the lobe has a FWHM of 0.044 m

Two horn antennas were made at the University of Manitoba since these were custom-made, 40 measurements per antenna were taken to find the phase delay. Again a linear fitting was done to match equation 2.4. For the custom horn antennas, there was a difference in performance between the antennas. For antenna A $p_1 = 1$ and $p_2 = 0.106$ m with an R square of 0.99. Figure 2-7 shows the 40 measurements along with the fitted line.

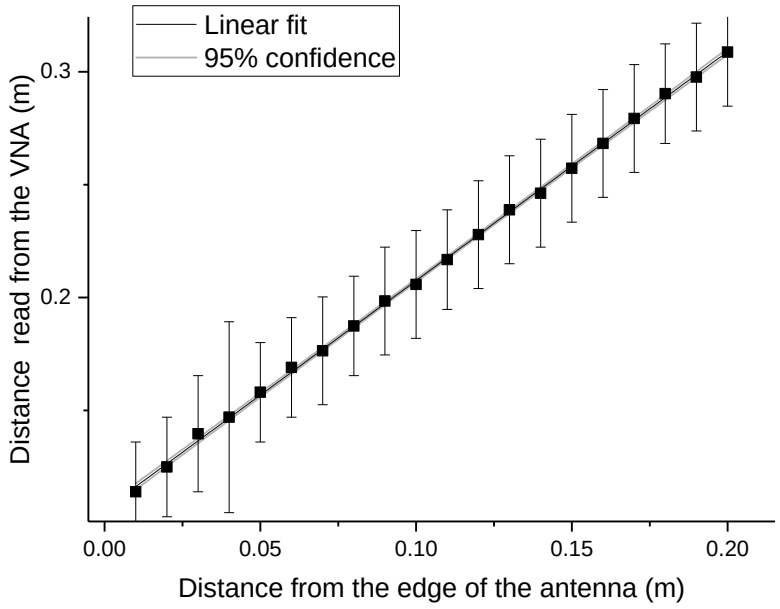

Figure 2-7 Data used to find the phase delay of the custom horn A. along with fitted line y=x+0.106, the error bars show the half-width of each of the measurements done

The second horn antenna (B) was also tested in the same fashion, with 40 measurements. After the linear fitting, the following results were obtained $p_1 = 1.013$ and $p_2 = 0.10$ m with an R square of 0.99. The experiment was repeated a few times with very similar results, Figure 2-8 shows the 40 measurements taken along the fitted line.

Antenna B had an intercept some 0.005 m smaller than antenna A, and returned less power. The result was consistent across different measurements (see Figure 2-9). Antenna A read approximately 20% more power under similar conditions. The discrepancy can be explained by considering that the antennas were custom-made, and as a result, it was hard to achieve consistency in the final manufacture.

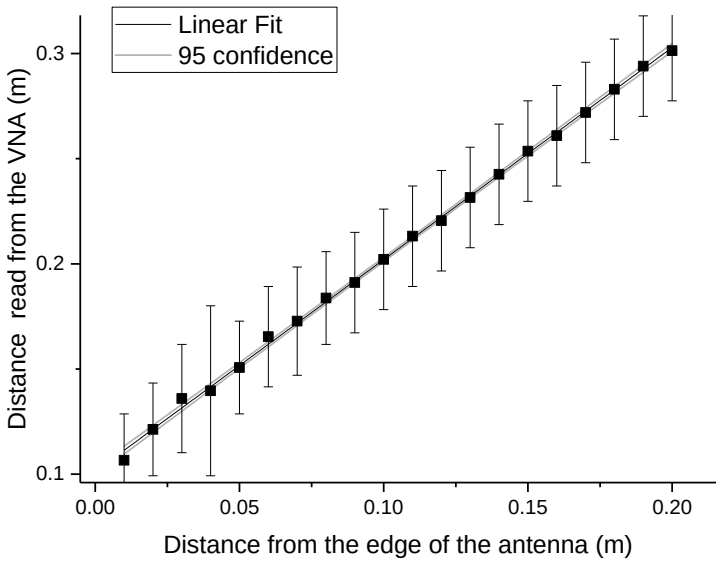

Figure 2-8 Data used to find the phase delay of the custom horn B. along with fitted line y=x+0.1 the error bars show the half-width of each of the measurements done

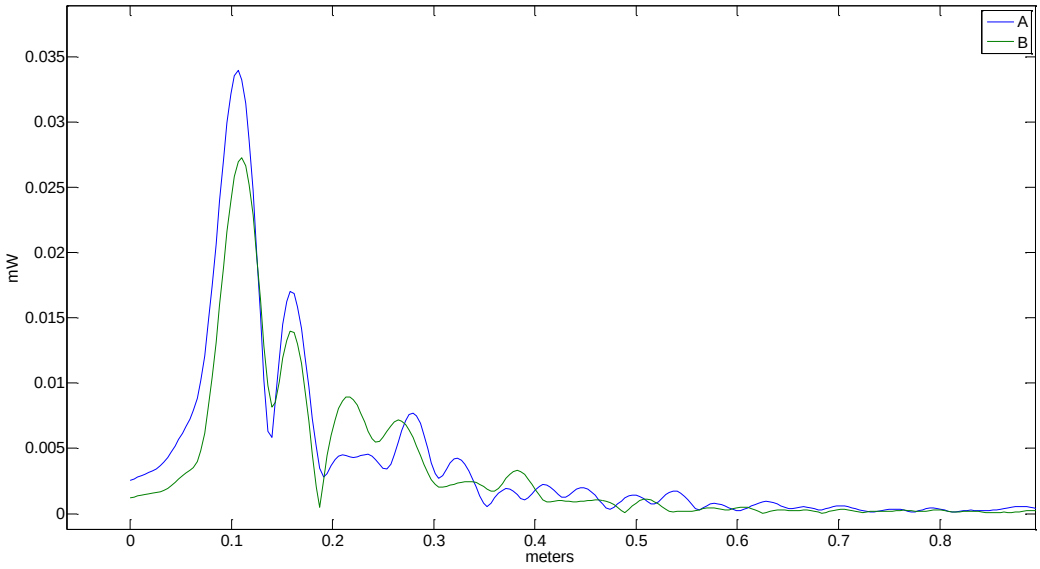

Figure 2-9 A comparison between the power received by antenna A and antenna B, with a metallic target at 0.01 m from the edge of each antenna. Antenna B shows a signal with 20% less power than antenna A. The power difference comes from the manufacturing process of the antennas, which did not meet specifications.

Three more experiments were performed with 20 samples each, to confirm that there is a consistent discrepancy between antenna A and B. The results are shown in Table 2-1.

	A	B	A	B	A	B
Slope (p_1)	0.994	1.019	1.004	1.006	1.007	1.019
Intercept (p_2) in m	0.109	0.102	0.109	0.103	0.109	0.102

Table 2-1 Phase delay of the custom horn antennas A and B, using equation $y = p_1 x + p_2$. 20 measurements where performed each time. A significant discrepancy in the intercept of 0.005 to 0.006 m is found between antenna A and B.

2.3.5 Commercial Horn Antennas

A pair of commercially available horn antennas (C and D) was bought to address the manufacturing difficulties from custom-made antennas. The antenna is made by A-INFO and is rated from 2 to 20 GHz with a gain of 12 dB (Figure 2-10 shows a -5 dB bandwidth of 1.58 to 8+ GHz). [25]

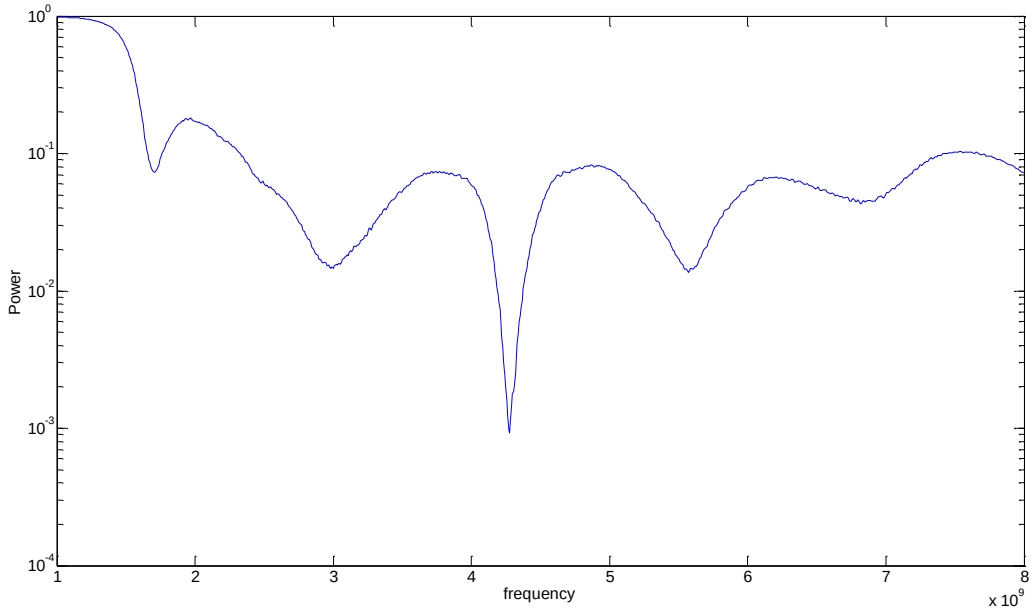

Figure 2-10 S11 response for the commercial horn antenna, with a -5 dB bandwidth of 1.58 to 8+ GHz

2.3.5.1 Commercial Horn Phase delay

We repeated the experiment described in section 2.3.2.1 for the commercial horn antennas.

Two antennas (C and D) were tested. Figure 2-11 shows the reflection obtained from a metallic plate at 0.01 m from the antenna. The difference in power from antenna C and D is only 5.3%.

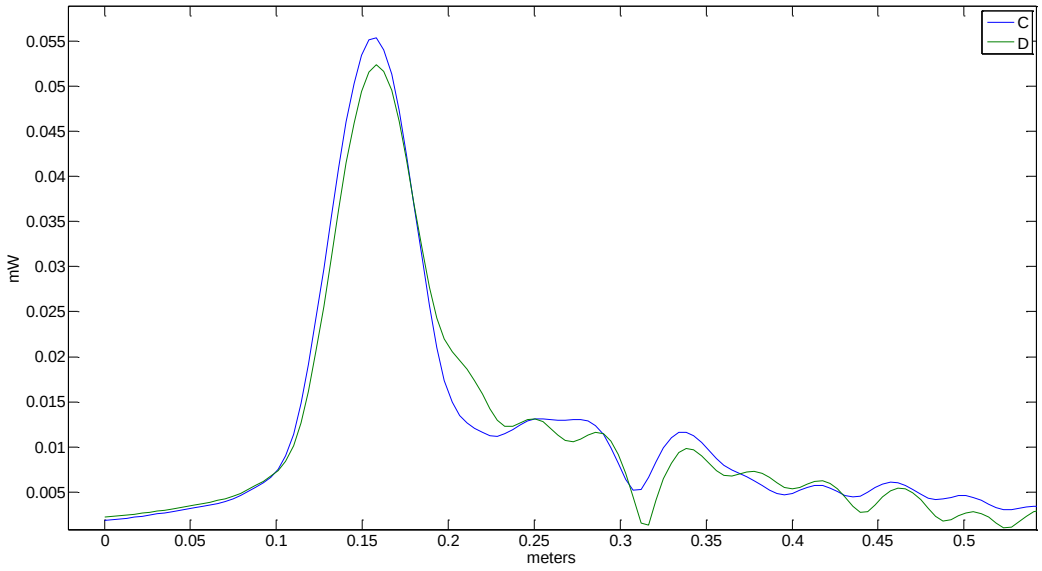

Figure 2-11 Comparison between the power received by antenna C and antenna D, with a metallic target at 0.01 m from the edge of each antenna, the power difference is 5.3%. Both main lobes have a FWHM of 0.057 m

24 measurements were taken to test the phase delay of both antennas. A linear fit was done following equation 2.4. For the commercial horn antennas, the performance was more similar. For antenna C $p_1 = 1.18$ and $p_2 = 0.148$ m with an R square of 0.99. For antenna D the interpolation yields $p_1 = 1.17$ and $p_2 = 0.148$ m with an R square of 0.99. Figure 2-12 and Figure 2-13 show the data points and fitted line.

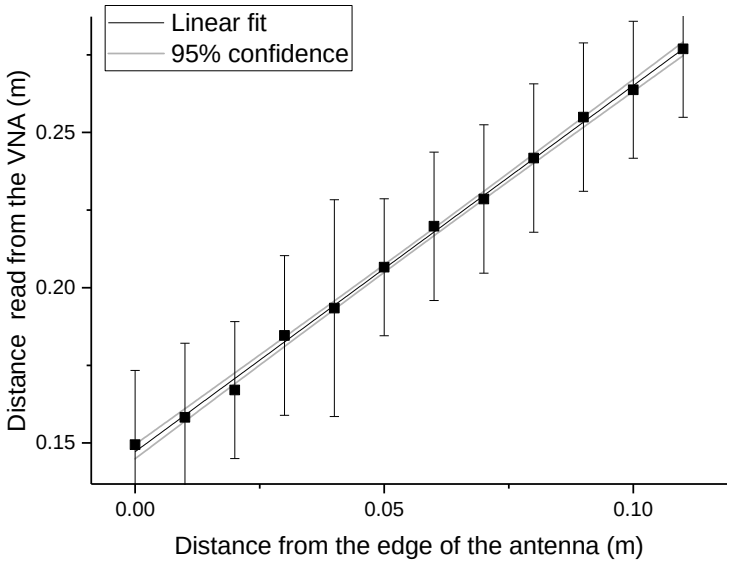

Figure 2-12 Data used to find the phase delay of the commercial horn C. along with fitted line y=1.18x+0.148

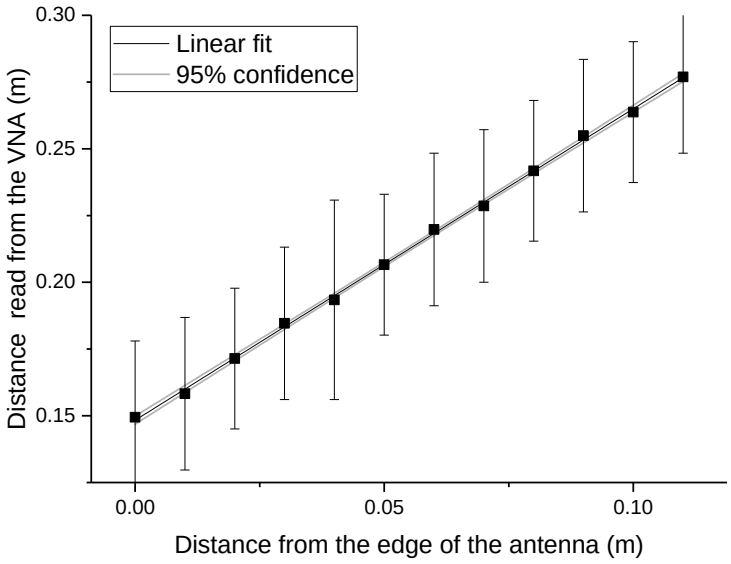

Figure 2-13 Data used to identify the phase delay of the commercial horn D. along with fitted line y=1.17x+0.148

All the experiments done up to this point were performed using a Fieldfox N9923A VNA and a range of 1 to 6 GHz. A second VNA from Copper Mountain was used to test antenna C with a wider bandwidth of 1 to 8 GHz. For this second test, the interpolation yields a $p_1 = 0.97$ and $p_2 = 0.148$ m with an R square of 0.99 using 17 data points. Figure 2-14 shows the data points used and the fitted line. The phase delay test was useful to identify the strengths of the commercial horn antennas, as they allow for a more consistent measurement across different experiments.

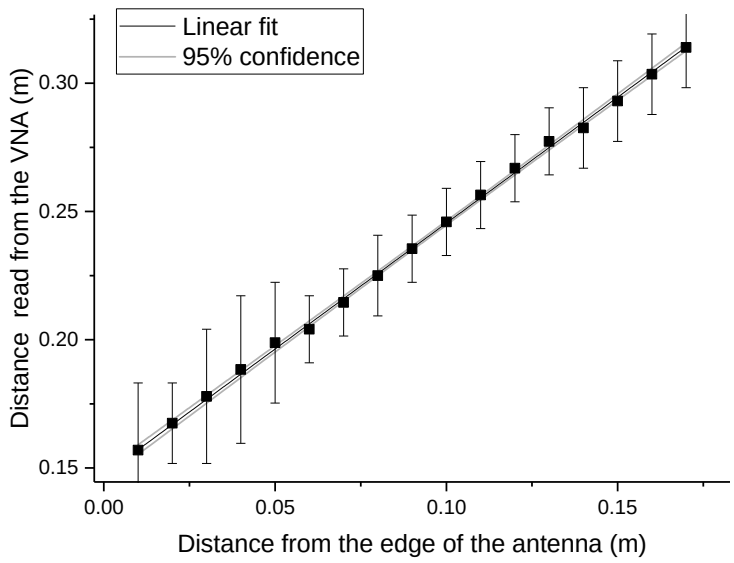

Figure 2-14 Data used to find the phase delay of the commercial horn C using a Copper Mountain VNA and a frequency range of 1-8 GHz. The data is fitted with a line y=0.97x+0.148

2.3.6 Antenna comparison using image quality metrics based on previous knowledge

2.3.6.1 Image metrics based on previous knowledge

A number of metrics were used to compare the performance of the antennas. These metrics are aided by previous knowledge of the region of interest. While the metrics may not be useful for a diagnosis, they aid in the comparison of test images where are the variables are known.

The signal to noise ratio (SNR) is a very common metric used to measure the sensitivity of a device. Generally, an SNR of at least 1 is needed to have a usable signal. There are many forms of SNR measurement; the power SNR was chosen since all our images show the power of the signal. SNR is a dimensionless measurement and is displayed in dB. Equation 2.6 shows how the SNR is calculated, where x_i is the signal of interest, and x_i' is the noise in the image.

$$SNR = 10\log_{10}\frac{\left(\frac{1}{n}\sum_0^n x_i\right)^2}{\left(\frac{1}{m}\sum_0^m x_i'\right)^2} \tag{2.6}$$

While the SNR is a very common measurement, when talking about radar systems the SNR has limited use. In radar systems, the noise is considered to be white and spread across the spectrum equally. However, the strongest interference comes from signals that have a strong presence in the region of the spectrum that the radar is working. Thus, an alternative measurement is the Signal to clutter ratio (SCR) where clutter is defined as all of the reflections that do not come from the target. In air to ground radar, clouds are considered a form of clutter. In BMR systems, the clutter comes from reflections of the air-skin boundary, the surrounding elements in the scan chamber, and the multi-path reflections. The SCR is calculated by dividing the strongest reflection from the signal by the strongest reflection from clutter [6, 26]

$$SCR = 10\log_{10}\frac{(Max\ tissue\ reflection)^2}{(Max\ clutter\ reflection)^2}. \tag{2.7}$$

We also compare the tumor to fibroglandular ratio (TFR). The TFR is obtained from the ratio of the tumor signal, and the fibroglandular tissue signal. TFR is helpful since the final objective of the system is to be able to distinguish between healthy tissue and tumors [28]

$$TFR = 10\log_{10}\frac{(Max\ Tumor\ Reflection)^2}{(Max\ Healty\ Tissue\ Reflection)^2}. \tag{2.8}$$

The SCR and TFR require knowledge of the phantom morphology. For this work, the SCR and TFR were calculated by identifying the areas that correspond to the locations of the tumor and fibroglandular tissue, and the rest of the image was assumed to be clutter. This means that there is some overlap between clutter and noise. Clutter comes mainly from the interface between the coupling medium and the phantom. In our experiments, the value of the clutter is greater than the noise by at least an order of magnitude.

2.3.6.2 Antenna comparison

To compare antenna gain a metallic sheet at 1 cm was used as a target for all antennas. All antennas follow the same set-up. Figure 2-15 shows the comparison between the three antennas. The Fieldfox VNA was used, and a frequency range of 0.02 to 6 GHz was used for the Vivaldi and custom horn antenna. The commercial horn was tested using a 1 to 6 GHz sweep.

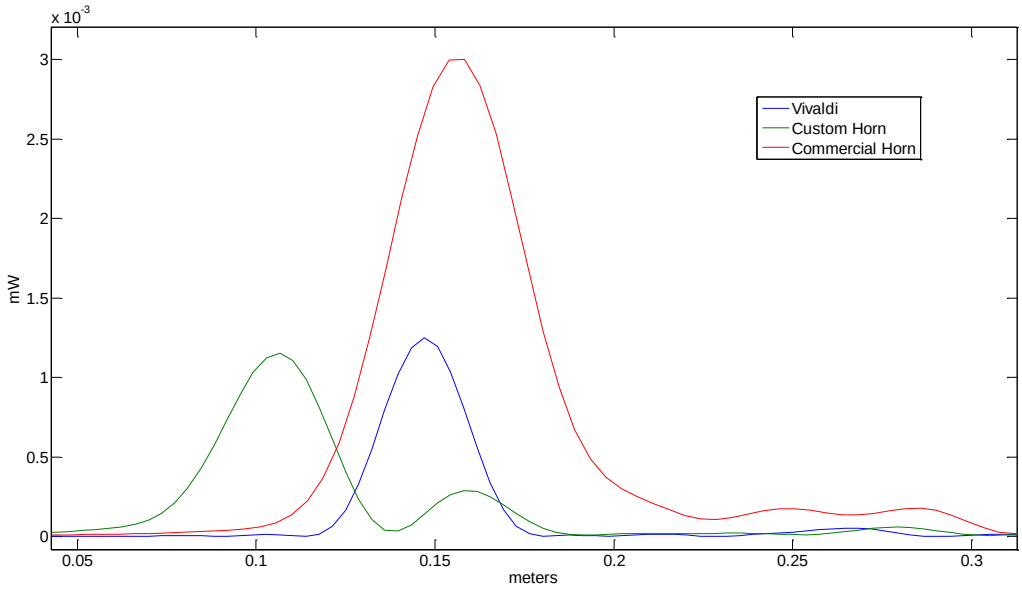

Figure 2-15 Comparison of the energy level received by the Vivaldi, custom horn, and commercial horn antenna. The target is a metallic sheet of 0.1 by 0.2 m at 0.01 cm from the edge of the antenna. The maximum response is 0.0339 mW for the Vivaldi, 0.0353 mW for the custom horn and 0.0548 mW for the commercial horn. FWHM was 0.037 m for the Vivaldi, 0.044 m for the custom horn, and 0.057 m for the commercial horn.

The commercial horn antenna has the biggest response with a magnitude of 0.0548 mW while the other two antennas have a response of less than half of that. The Vivaldi antenna has a response of 0.0353 mW while the custom-made horn has one of 0.0339 mW. The disadvantage of the commercial horn antenna is that it has a wider lobe, and thus it may be harder to separate two different objects when they are closer together. The commercial horn antenna has a bandwidth from 2 to 20 GHz while the other two antennas have a bandwidth that starts at a lower value (1.5 GHz for the custom horn, 1 GHz for the Vivaldi). The difference in the bandwidths is one explanation

for the differences in the main lobe width. After the VNA was upgraded to one that supports up to 8 GHz the width of the main lobe of the commercial horn was lower. The upgraded VNA is a planar 804/1 from Copper Mountain. Figure 2-16 shows the response of the commercial horn antenna when paired with the planar VNA and using an extended bandwidth of 1 to 8 GHz.

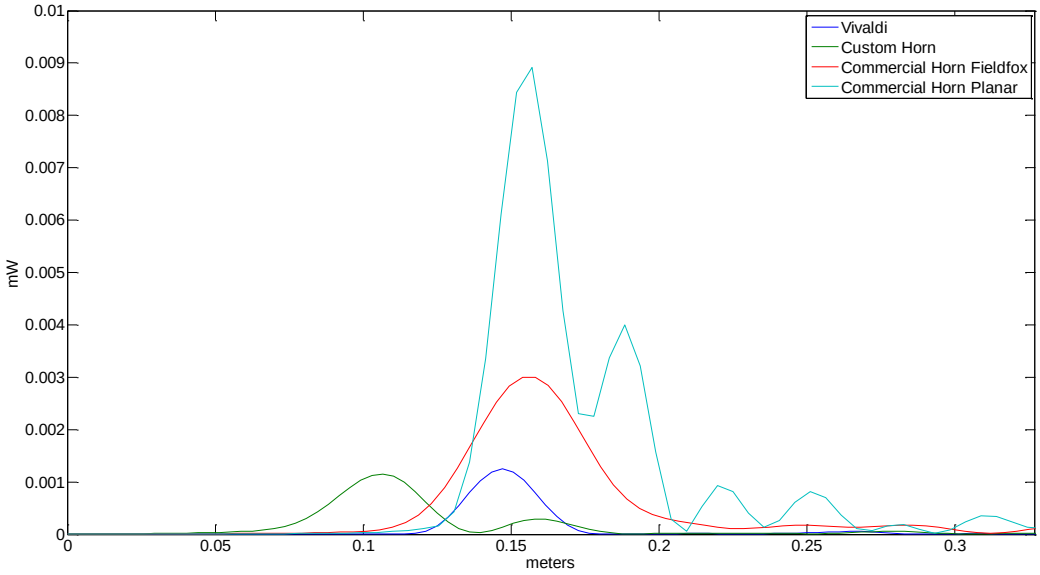

Figure 2-16 When paired with a VNA with higher bandwidth the commercial horn antenna performs better. The magnitude of the reflection is 0.0944 mW, and the FWHM is 0.0314 m.

The Planar 804/1 VNA has a maximum output power of 10 dBm (decibel- milliwatts) while the Fieldfox N9923A VNA has a maximum output power of 5 dBm. The higher output power explains why the commercial horn antenna has a stronger reflection with the Copper Mountain VNA. The signal taken with the Planar has a narrower main lobe (0.0314 m FWHM when compared to 0.057 m). While there is not a direct correlation between bandwidth and FWHM, this result does indicate that bandwidth is one of the factors that affect the FWHM.

Expression 2.4 shows how the range resolution of the system (Δx) is related to the bandwidth. With higher bandwidth the system can detect between two different targets that are closer together. Expression 2.4 explains the results of Figure 2-16 where the higher bandwidth generates a narrower

lobe with the same target. The bandwidth is affected by the VNA and the antenna used. While the bigger bandwidth would allow for higher resolution, the higher frequencies may not penetrate the breast tissue.

To test the custom horn and Vivaldi antenna, a 56 x 56 x 40 cm^3 tank made of Plexiglas was used, where the antennas were secured to a lid. The antennas were tested with a glycerin phantom in a styrene-acrylonitrile cylinder with a diameter of 13 cm and a height of 35 cm. To simulate the fibroglandular tissue, a synthetic polymer (TX-151) mixed with distilled water was used. A saline solution was used to match the dielectric properties of tumor-like structures inside the breast. The antennas were also tested using canola oil as a coupling medium and were compared to the performance when there is no coupling medium present. Table 2-2 shows the relative permittivity of the materials used and a comparison with the breast tissue. [30,31]

Material	**ε_r(3 GHz)**	**Material**	**ε_r(3 GHz)**
Low-density breast tissue	9	Glycerin	7.29
Fibroglandular tissue	25-37	TX-151 polymer	35
Tumor	55	Saline mixture	53
Styrene-acrylonitrile	2.5	Canola oil	2.6
Cellulose acetate butyrate	2.9	Water	76.3

Table 2-2 Relative permittivity of the materials used for the phantom in the experiments done [30].

A phantom with two fibroglandular-like targets was set-up. The targets are 90 degrees apart, and position at 4.5 cm from the center of the scan rotation. Later experiments added a tumor-like structure to one of the TX-151 targets. Figure 2-17 shows the diagram of the phantoms used to test the Vivaldi and horn antenna.

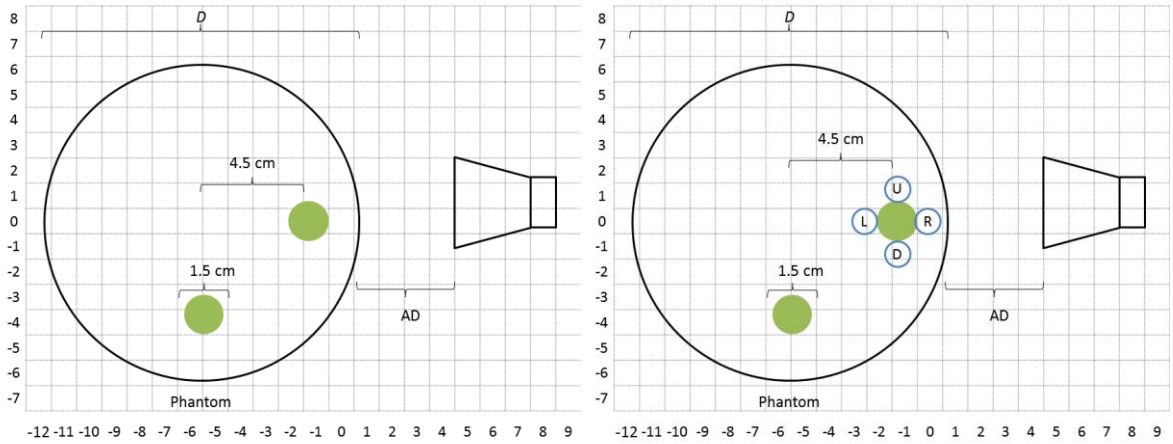

Figure 2-17 Set-up for a test of the Vivaldi and horn antennas. The distance D=13 cm while the distance AD=5 cm for the Vivaldi antenna and AD=4 cm for the custom horn antenna. One set-up is two fibroglandular like targets (TX-151). The second set-up has a tumor-like structure attached to a fibroglandular target. The tumor was placed in four different positions (R, D, L, and U). This setup was used with oil and air as a coupling medium

An initial set of ten experiments, five for each antenna, were performed. The experiments were performed in air and with a glycerin phantom. Both phantoms have the same characteristics.

An analysis is performed using the raw data (i.e. before reconstruction) obtained from the VNA in the time domain. For complex phantoms, it would be impossible to gather much insight from the raw data. The experiment uses simple, two targets, phantoms where the position of all the elements is known. An analysis of the raw data can be done using the information of the target position. Figure 2-18 shows how a simple two target set-up creates a set of sinusoidal projections in the time domain.

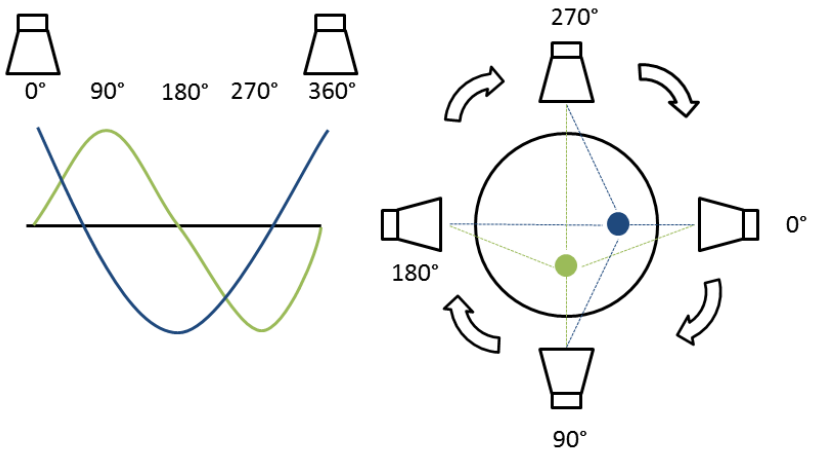

Figure 2-18 When the antenna rotates around a simple point-like target the projection generated is similar to a sinusoidal signal, where the points closer to the antenna produce a greater reflection. The black line is positioned at the radius of the scan geometry.

Based on the diagram from Figure 2-18 a set of image quality metrics (SNR, SCR, TFR) is used to analyze the data. Raw data analysis is useful to avoid any inconsistency or issue that a reconstruction may introduce. The analysis done is using the metrics introduced in section 2.3.6.1. Figure 2-19 shows the raw data obtained from the set of 10 initial experiments. Due to the attenuation of the glycerin, only a few points on the sinusoidal graph are visible in the image, but a good reconstruction would take advantage of the frequency domain data to increase the detail.

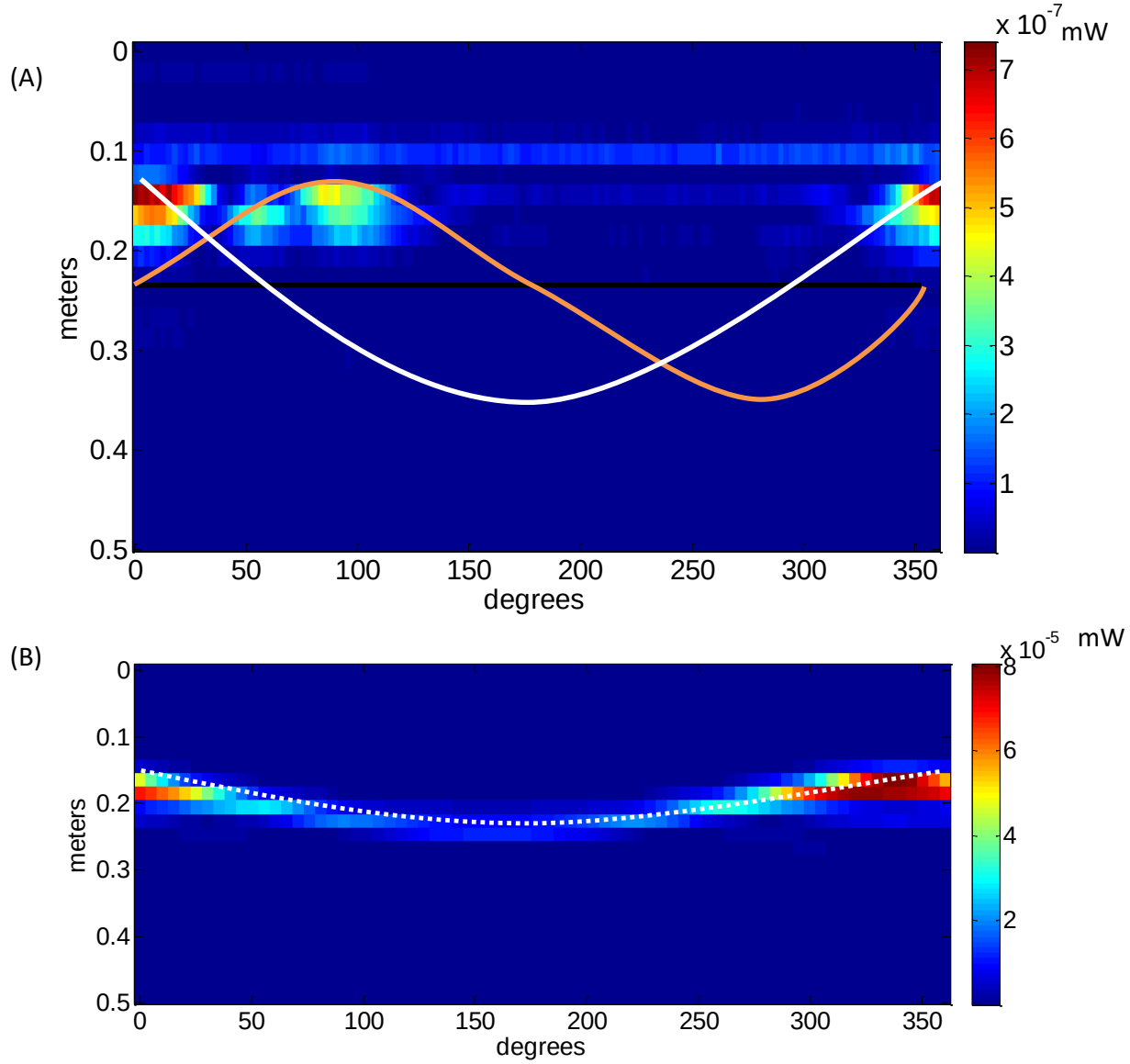

Figure 2-19 (A) Raw data in the time domain obtained from a phantom of 2 fibroglandular targets. No tumor target is present. The Phantom follows the set-up from Figure 2-17. (B) Shows a simpler phantom with only one target, this was taken in air and allows for a better display of the target path. Both data sets taken with the custom horn antenna.

Vivaldi antenna				Custom horn antenna			
	SNR (dB)	SCR (dB)	TFR (dB)		SNR (dB)	SCR (dB)	TFR (dB)
No tumor	13.5 (±1.3)	4.5 (±1.2)	NA	No tumor	16.2 (±0.8)	4.8 (±0.7)	NA
Tumor at R	13.1 (±1.3)	7.0 (±1.2)	5.7 (±1.2)	Tumor at R	24.3 (±0.8)	17.0 (±0.7)	28.9 (±0.7)
Tumor at D	11.7 (±1.3)	4.8 (±1.2)	-5.9 (±1.2)	Tumor at D	16.7 (±0.8)	7.0 (±0.7)	10.5 (±0.7)
Tumor at L	10.7 (±1.3)	4.6 (±1.2)	-5.6 (±1.2)	Tumor at L	13.3 (±0.8)	3.2 (±0.7)	8.4 (±0.7)
Tumor at U	10.3 (±1.3)	2.4 (±1.2)	2.2 (±1.2)	Tumor at U	16.6 (±0.8)	7.9 (±0.7)	17.9 (±0.7)

Table *2-3 Results of the analysis performed on the raw data obtained from the initial ten experiments. The phantom is shown in Figure 2-17, and the tumor like target is moved to different positions. This is done with air as a coupling medium, and a glycerine phantom.*

Table 2-3 is a summary of the results obtained from the initial set of 10 experiments. The custom horn antenna shows a better performance in SNR, SCR, and TFR and in general shows a higher response from the targets. The custom horn antenna has a higher gain. The Vivaldi antenna shows some negative values in the TFR measurement because the fibroglandular response is greater than the tumor response. When the tumor is in position D or L is harder to get a response from it. In position L, the tumor is behind the fibroglandular tissue and it is harder to get a response from it when the signal has to travel through the fibroglandular target. In position D, the tumor is hidden in responses from the second target. Since the Vivaldi antenna has a broader radiation pattern, the signal obtained from the second target may obscure the tumor.

The same analysis was done on the reconstructed images. Table 2-4 shows a summary of the analysis when performed in reconstructed data. The reconstructed images show an improvement in the SNR of the Vivaldi antenna when compared with the raw data. The custom horn antenna still performs better in the TFR measurement. When the tumor is at D and L the Vivaldi antenna has a negative TFR, meaning the tumor may be lost to diagnosis.

Vivaldi antenna				Custom horn antenna			
	SNR (dB)	SCR (dB)	TFR (dB)		SNR (dB)	SCR (dB)	TFR (dB)
No tumor	19.0 (±0.9)	7.0 (±0.6)	NA	No tumor	16.6 (±1.2)	5.0 (±0.4)	NA
Tumor at R	19.6 (±0.9)	7.7 (±0.6)	10.8 (±0.6)	Tumor at R	21.3 (±1.2)	13.1 (±0.4)	21.7 (±0.4)
Tumor at D	19.4 (±0.9)	7.1 (±0.6)	-0.4 (±0.6)	Tumor at D	14.2 (±1.2)	9.2 (±0.4)	11.6 (±0.4)
Tumor at L	19.2 (±0.9)	7.0 (±0.6)	-8.4 (±0.6)	Tumor at L	11.1 (±1.2)	4.9 (±0.4)	4.1 (±0.4)
Tumor at U	18.0 (±0.9)	7.1 (±0.6)	2.9 (±0.6)	Tumor at U	13.5 (±1.2)	9.2 (±0.4)	14.3 (±0.4)

Table 2-4 Results of the analysis performed in the reconstructed data obtained from the initial ten experiments. The TFR is better for the horn antenna across all measurements. The phantom is shown in Figure 2-17, and the tumor like target is moved to different positions. Tumor at R position (closest to the antenna), tumor at D position (side of the fibroglandular patch), tumor at L position (behind the fibroglandular target), tumor at U position (side of the fibroglandular patch). This table shows the results for air as a coupling medium and a glycerin phantom.

Figure 2-20 shows the reconstructed image of the ten experiments performed to compare the Vivaldi and custom horn antenna. The Vivaldi antenna has a cleaner image (reflected by the more stable SNR). The horn antenna has a ring of clutter that comes from the interface air-glycerin. This

clutter is not present in the Vivaldi antenna. The horn antenna has the advantage of having a stronger response coming from the tumor. When the tumor is at the L position the horn antenna shows a higher cross-section for the tumor. The Vivaldi antenna shows a higher energy response from the fibroglandular target.

The horn antenna shows a stronger response in the targets where the tumor is present (this is also reflected in the TFR measurement). When a tumor is added, even if it is hidden behind a fibroglandular target, the response is higher when compared to a fibroglandular tissue alone. Base in these measurements it is safe to assume that the tumor generates a stronger reflection even when hidden for the horn antenna.

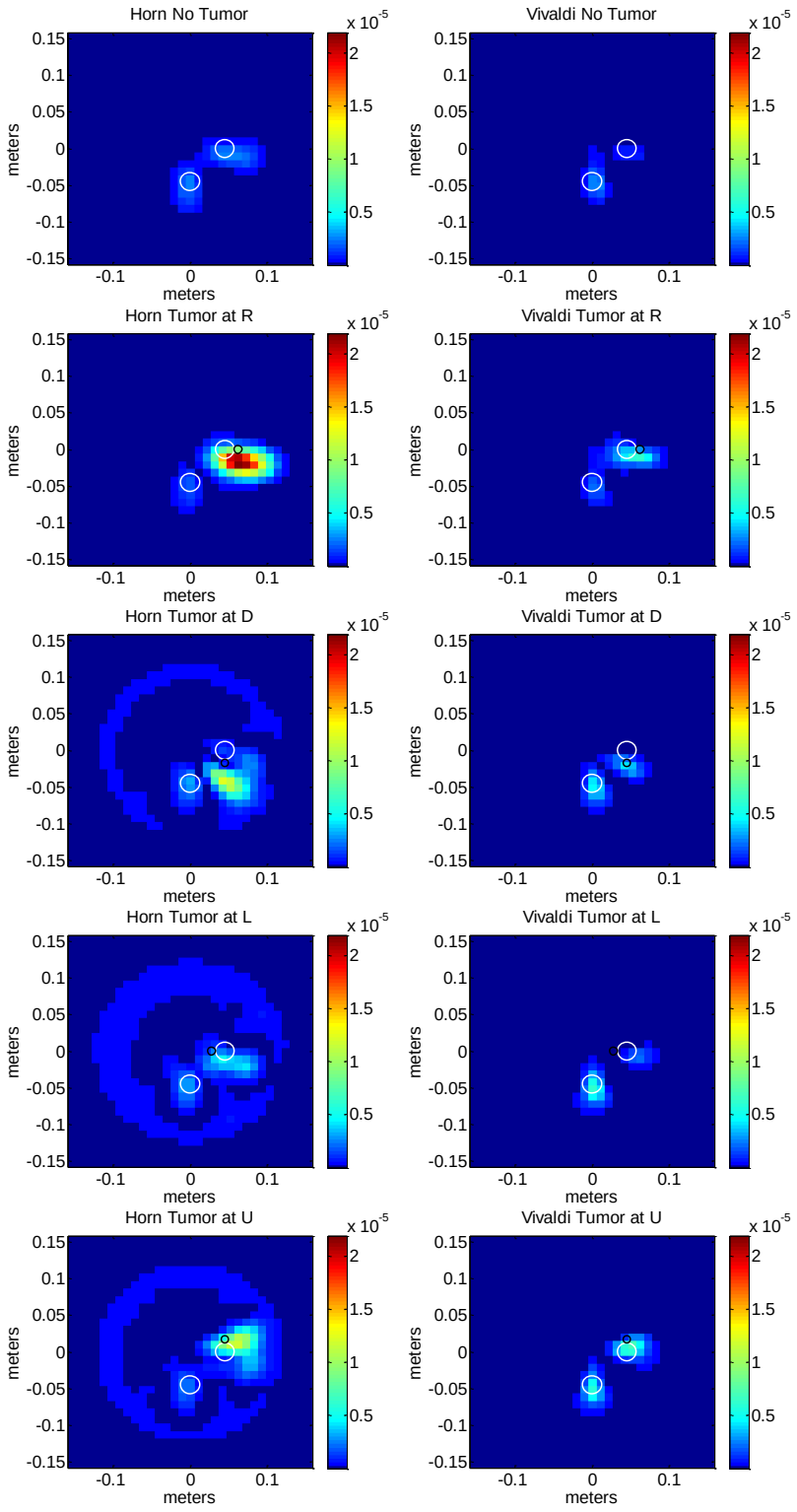

Figure 2-20 Ten experiments used to compare the Vivaldi and custom horn antenna. The power scale is in mW and is the same scale for all ten images. The white circle shows where the fibroglandular tissue is while the black circle shows where the tumor was located. The experiments were performed in air and with a glycerin phantom.

Chapter 4 presents a longer discussion on the type of filters used in the data for reconstruction. Due to the scan geometry, there is an oversampling in the center of the image. The points reconstructed further away from the center are under-sampled, and an interpolation is carried out, as mentioned in Section 1.3.4.2 to resolve the uneven sampling. The power of the image is modified by the interpolation and the filters used in the data before reconstruction. To maintain consistency, the output data obtained in the reconstructed image is multiplied by a factor proportional to the energy of the input data.

A new set of experiments was performed using canola oil as a coupling medium. A special casing was design to keep oil from entering the interface between the antenna and the cable. The set of experiments follows the same set-up as Figure 2-17. Five experiments were done with the Vivaldi antenna, and five with the custom horn antenna. Table 2-5 summarizes the results of the experiments.

Vivaldi antenna				Custom horn antenna			
	SNR (dB)	SCR (dB)	TFR (dB)		SNR (dB)	SCR (dB)	TFR (dB)
No tumor	17.9 (±0.6)	5.6 (±0.4)	NA	No tumor	16.0 (±1.1)	7.1 (±0.5)	NA
Tumor at R	16.6 (±0.6)	5.2 (±0.4)	3.4 (±0.4)	Tumor at R	13.2 (±1.1)	4.8 (±0.5)	3.6 (±0.5)
Tumor at D	15.9 (±0.6)	3.5 (±0.4)	-5.2 (±0.4)	Tumor at D	16.4 (±1.1)	7.2 (±0.5)	11.5 (±0.5)
Tumor at L	17.4 (±0.6)	5.0 (±0.4)	1.3 (±0.4)	Tumor at L	15.7 (±1.1)	7.2 (±0.5)	10.9 (±0.5)
Tumor at U	15.5 (±0.6)	4.7 (±0.4)	0.9 (±0.4)	Tumor at U	16.3 (±1.1)	7.3 (±0.5)	9.5 (±0.5)

Table 2-5 Results of the analysis performed in the reconstructed data obtained from the ten experiments with oil. The phantom is shown in Figure 2-17, and the tumor like target is moved to different positions.

In the experiments with canola oil the Vivaldi antenna has a low to negative TFR while the custom horn antenna has a TFR that on average is 8 ± 5 dB higher than that of the Vivaldi. The SNR and SCR of both antennas are similar, at -1 ± 2 dB and 2 ± 2 dB respectively. When comparing table 2-4 with table 2-5 the highest TFR is shown to be in the horn antenna without coupling medium. As explained earlier, the SNR can be a poor way of comparing two radar images (particularly with an SNR above 5 dB). The TFR is more relevant for BMI scenarios since it shows how well the system can

discriminate between fibroglandular tissue and tumors. As discussed in Section 1.2 the contrast between fibroglandular tissue and malignant tissue is the bias for BMI. A good microwave imaging system would make use of such contrast as much as possible.

The commercial horn antenna experiments were performed with an updated microwave system. The datasets were generated using a Copper Mountain VNA (planar 804/1) that has a higher frequency range and higher output power. The system is now designed to scan patients and consist of a bed frame that supports a padded surface. The antennas are housed inside the bedframe, where a motor rotates the antennas the VNA and the needed power supplies. A second motor is capable of moving the antennas in the Z direction (the previous system was limited to the XY plane). The antennas are housed inside a chamber with radar absorbent material (RAM) to avoid any interference from the outside or reflections from the metal bedframe.

The phantom was also improved to allow for a closer approximation to a real breast. The previous phantom was a cylinder; the new phantom follows the shape of a breast. The new phantom is made of cellulose acetate butyrate (CAB). The phantom is supported in the bedframe in the same position that a patient would lie down for a scan in the system. The commercial horn antennas are designed to be used in air, and no coupling medium was tested.

The experiments for the commercial horn were all done in the bed system. Some of the differences between the commercial horn and the custom-made antennas come from the changes in the system, a larger bandwidth and a higher output power.

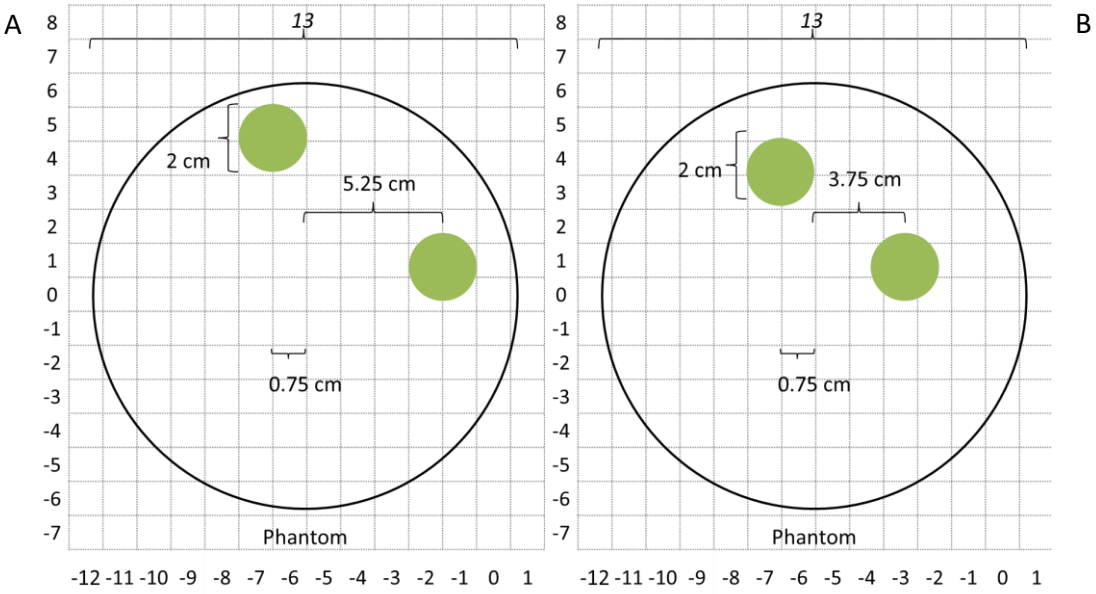

Figure 2-21 The commercial horn antenna was tested using a two target set-up. A set-up is two targets at 5.25 cm from the center, while B set-up is 3.75 cm from the center. Both targets are similar to a fibroglandular tissue structure.

The set-up shown in Figure 2-21 was used to test the commercial horn antenna. The experiments were repeated using a mixture of water and glycerin. Glycerin has a $\varepsilon_r = 7.3$ while water has a $\varepsilon_r = 76.3$. A mix of *water and glycerin* is used to control the relative permittivity of the phantom. For a mixture of 10% water 90% glycerin $\varepsilon_r = 8.73$, for 20% water 80% glycerin $\varepsilon_r = 13.71$

100% Glycerin				90% Glycerin 10% water			
	SNR (dB)	SCR (dB)	TFR (dB)		SNR (dB)	SCR (dB)	TFR (dB)
No tumor	16.0 (±1.2)	7.9 (±0.4)	NA	Set-up A	18.2 (±1.2)	5.6 (±0.4)	NA
Tumor at R	15.5 (±1.2)	7.0 (±0.4)	8.0 (±0.4)	Set-up B	17.4 (±1.2)	2.9 (±0.4)	NA
100% Glycerin				80% Glycerin 20% water			
Set-up A	18.6 (±1.2)	5.0 (±0.4)	NA	Set-up A	14.2 (±1.2)	3.0 (±0.4)	NA
Set-up B	18.8 (±1.2)	4.9 (±0.4)	NA	Set-up B	12.5 (±1.2)	1.6 (±0.4)	NA

Table 2-6 Results of the commercial horn test. The no tumor and tumor at R follow the phantom in Figure 2-17. The set-up A and B follow the phantom shown in Figure 2-21. In this case, the phantom was filled with glycerin and the antennas were in air.

Table 2-6 shows the results of the experiments for the commercial horn antenna. It is hard to compare the commercial horn antenna with the previous antennas using these results. The SNR of both types of horn antennas is close considering the uncertainty, and there is not enough data to

compare the TFR. The commercial horn has a higher gain (as shown in Figure 2-15). However, the bed system is a more challenging imaging environment, since the antennas rotate (the previous system rotated the phantom), and the breast phantom and patient tissue structures are more complex.

While the SNR for the commercial horn stays above the 10 dB, the SCR drops significantly when a mixture with higher permittivity is used. When a mixture of 90% glycerin and 10% water was used a drop of SCR from set-up A to set-up B was registered. Set-up A has the fibroglandular targets closer to the wall of the phantom, and thus, the signal has to travel less inside the high loss mixture of glycerin and water. The deeper the target, the harder it is to get a signal back.

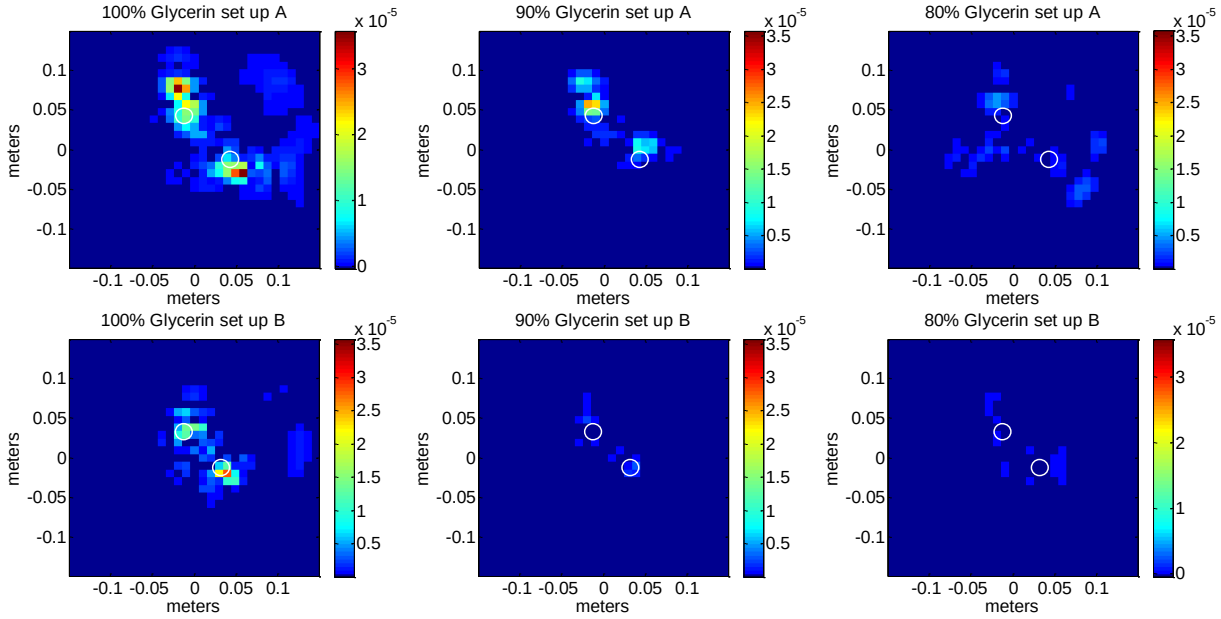

Figure 2-22 Set of experiments for the commercial horn antenna. The power scale is in mW and is the same scale for all ten images. The white circle shows where the fibroglandular tissue was located. The experiments were performed in air and with a glycerin phantom.

Figure 2-22 shows six images from table 2-6. Since the images share the same power scale some of the detail is lost due to the dynamic range. While the SNR may be high, the SCR is a better indicator of the quality of the images. Set-up B for the mixture of glycerin at 90% and 80% have a low SCR;

this is reflected in the image where is harder to discern the targets from the background. In the case of the lowest SCR of 1.55, it may not be possible to find the targets without a prior knowledge of the phantom.

The objective of the bed imaging system is to be used in clinical trials. This system was already used successfully with volunteers where the main objective was to report if the patient is comfortable and safe. Some suggestions were provided by the volunteers during the safety trial. These suggestions are being implemented to prepare the system for a clinical trial in a hospital environment.

Selecting the right antenna for the imaging system is a challenging task. Custom-made antennas offer the advantage of flexibility in the specifications. The custom-made horn antennas were smaller in size and could be submerged in oil. The disadvantage is that there is a higher variability between antennas. If an antenna is replaced, the new one has to be characterized again to compensate for any variance in the specifications. Commercial antennas allow one antenna to be characterized since subsequent antennas are within a small margin of error of the specifications. Custom-made antennas are more expensive and require a longer development time when compared to off the shelf antennas.

Figure 2-16 shows the advantages of the commercial horn antenna. It has a higher gain, and the higher bandwidth allows for a better resolution. Experiments performed with phantoms are less conclusive. It is important to note that due to time constraints the commercial horn was only tested in the bed system. The custom-made horn antenna was only tested using the old bench top system with simpler phantoms.

The results presented indicate that the use of oil as coupling medium does not provide an advantage over air. The results show that using a coupling medium does not improve our ability to detect a tumor, as demonstrated by the TFR results in Tables 2-4 and 2-5. A better VNA (higher power and better dynamic range) may be able to improve the images when using a coupling medium. Using oil will also increase the design challenges of the imaging system. The bed system was designed to be used without any coupling medium, to allow for a more robust mechanical design.

2.4 VNA characteristics

The VNA in our system was used to generate and record the transmitted signals. As shown in Figure 2-16, using a VNA with better specifications can yield a better response using the same antenna/set-up. A better VNA often comes with a higher price.

The dynamic range of the VNA is the difference between the smallest and largest signal that the VNA can measure using the same configuration. A large dynamic range allows us to record attenuated signals from inside the breast. The dynamic range was reported by the manufacturer of the VNA. The instantaneous linear dynamic range (ILDR) is defined by the largest signal that can be detected and the measurement floor as defined by the system noise and the nonlinear products of the larger signal. The ILDR is also affected by factors independent of the VNA (antenna type, ambient noise, cable type).

For the imaging system, two different VNAs were tested. The Fieldfox N9923A is a handheld VNA that is compact and does not require a computer to be operated. The Fieldfox N9923A operates in the frequency range of 2 MHz to 6 GHz and has an output power of 5 dBm (3.2 mW). It has a dynamic range of 100 dB. The Planar 804/1 is a VNA made to be rack mounted and can only be

controlled by a computer. It operates from 300 KHz to 8 GHz. The output power is 10 dBm (10mW), and the dynamic range is 150 dB.

While a full comparison of both VNAs was not made, the previous section shows some of the strengths of the Planar 804/1 VNA. Figure 2-16 indicates that using a higher output power and higher bandwidth make an improvement on the received signal.

2.5 Conclusion

The current chapter shows the strengths and limitations of the different hardware used for BMI. A custom antenna allows for specifications that are a better fit for breast microwave imaging. Often there are space limitations for the antennas, and the use of a coupling medium may be desirable. The disadvantage of custom hardware is the variance of the specifications between antennas.

Chapter 1 presents some examples of BMI systems that use a coupling medium. However, for the system used in this work, it is hard to justify the use of a coupling medium. The main coupling medium tested was oil, and the image analysis shows that there is little advantage of using it. The use of a liquid coupling medium also presents design challenges for the system. Additional care has to be taken to avoid any spills of the coupling medium outside the scan chamber.

When comparing VNAs the specifications provided by the manufacturer are important, but it is also necessary to consider the application. For the Planar 804/1, a computer is required to operate the VNA. While Copper Mountain provides extensive libraries to program the VNA, the libraries are limited to the Windows operating system. This is in contrast to the Fieldfox VNA that can be controlled over Ethernet using a simple TCP/IP connection, allowing it to be controlled by a more diverse range of hardware, like a microprocessor or a Linux computer. This makes the Fieldfox a

more compelling option for a portable system, despite the reduce bandwidth and lower power output.

Independently of the type of VNA used it is important to consider that the equipment has to be calibrated every time there is a drift on the results. A warm up period has to be observed to allow for a thermal equilibrium. A final system that is used in a hospital setting would have to integrate a self-calibrating option that can be performed by medical staff.

This chapter lays the foundation for the analysis done in the following sections. The image metrics allow for a consistent analysis through the chapters. The hardware described in this Section is the same used in the following Chapters.

The comparison between antennas informed the design decisions of a clinical system. Earlier versions of the BMI system used in the non-ionizing imaging lab had oil as a coupling medium. For the clinical system having oil as a coupling medium would pose additional mechanical challenges. It would also increase the discomfort of the volunteers. There are compromises to be made when choosing between oil and air as a coupling medium, and knowing the characteristics of the antennas, allows a better understanding of said compromises.

3 Sampling constraints for BMI in a circular scan geometry.

3.1 Introduction

The current microwave imaging system (MIS) uses circular scan geometry, as shown in Figure 3-1. This morphology allows the illumination of malignant lesions in the upper quadrants of the breast, which is the location where the majority of breast tumors originate [17]. The current work is presented using only monostatic data from the system, but the system is set to enable a bi-static configuration to be utilized in the future.

A monostatic scan uses one antenna for the scan. The antenna sends the signal and records the reflections at the same position. A bi-static approach uses two antennas for a scan. One antenna sends a signal to the ROI, and both antennas record the reflections. A bi-static approach has the advantage of recording scatter reflections at different angles than the incident one.

In Section 2.3.1 a discussion of the range resolution of a radar-based reconstruction is presented. A high bandwidth would allow for a high range resolution. A 6 GHz bandwidth would yield a resolution of 2.5 cm in air. It is desirable to have the same resolution in the cross-range, but it is harder to achieve (Figure 4-6 shows the range and cross-range direction for a circular scan geometry). The cross-range resolution is reliant on the number of scan positions, the beamwidth pattern of the antenna and the multipath reflections that may introduce clutter.

For the MIS the beamwidth of the antennas covers the full ROI. This facilitates the calculations for the number of scan positions needed. A reference scan with an empty chamber is used to eliminate multipath reflections. Radar absorbent material is also used to shield the metallic supports of the system. This means that the cross-range resolution depends on the number of scan positions in the MIS.

The number of scan positions for our system impacts the scan time linearly above 36 locations. The current bed system is set up to allow for up to 288 scan positions around the ROI for any plane. A high number of scan angles has the advantage of capturing more data, but every additional scan location adds an average of 11.7 seconds to the scan time. Phantom studies may not be impacted by scan time, but when a volunteer is being scanned, a long wait can cause discomfort or an unwanted movement.

The current chapter explores both, a theoretical criterion, and a practical approach to determining the minimal number of scan locations. First, the signal model analysis is presented, where based on the scan geometry, a condition is obtained that determines the minimal number of scan locations. In Section 3.3, a set of experiments was used for experimental validation. The results are compared with the theoretical expectation and analyzed using the metrics of Section 2.3.6.1.

3.2 Signal model analysis

The range direction of a radar system is parallel to the signal travel, while the cross-range direction is perpendicular to the range. The cross-range direction is also called slow-time direction since the movement of the antennas in the cross-range is slower than the travel time of the wave being used. Fast time refers to the range direction following the same convention [6].

The MIS consist of a circular scan geometry with a radius *R* and *M* scan locations. A waveform $f(t)$ with a bandwidth *B* is radiated into the scan region from the scan location at (R, θ) and the reflections from the scan region are recorded at M receiving locations. The collected response on the scan location at (R, φ) is given by:

$$s(t, \theta, \varphi) = \sum_{q=1}^{T} \gamma_q(\theta, \varphi) f(t - \frac{D_q(\theta) + D_q(\varphi)}{c_n}), \quad (3.1)$$

where $D_q(\theta) = \sqrt{R^2 + r_q^2 - 2Rr_q \cos(\phi_q - \theta_j)}$, R is the radius of the scan geometry, and (r_q, ϕ_q) are the polar coordinates of the q^{th} target. T is the total number of scatter objects. c_n is the speed of the wave in the medium. $\gamma_q(\theta, \varphi)$ represents the radar cross section function of the q^{th} object. The radar cross section is affected by the dielectric properties and shape of the target. Figure 3-1 shows a diagram of the scan geometry with the positions marked [33 34].

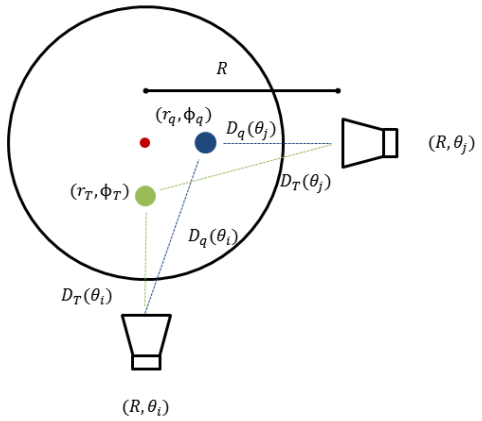

Figure 3-1 Scan geometry of the microwave imaging system. Every scan position is at (R, θ_n) where θ_n is the angle of the scan geometry and R is the radius of the scan geometry. Every target is at coordinates (r_n, ϕ_n) and $D_n(\theta_n)$ is the function of the distance from the scan position to the target.

The spherical phase function (SPF) represents the impulse response of the imaging system [29]. The SPF can be obtained by a Fourier transform of the recorded response. For the MIS the transmitted signal f(t) has a delay by a factor of $\frac{D_q(\theta)+D_q(\varphi)}{c_n}$ or $\frac{2\,D_q(\theta)}{c_n}$ when the transmitter antenna is the same as the receiving antenna. By applying the shift theorem of the Fourier transform, the SPF becomes:

$$s(\omega, \theta, \varphi) = \sum_{q=1}^{T} \gamma_q(\theta, \varphi) F(\omega) \exp\left(-jk\left(D_q(\theta) + D_q(\varphi)\right)\right), \quad (3.2a)$$

where $k = \omega/c_n$, also known as the wave number. The radar response has two modulations, one affected by the speed of travel of the wave in the range direction, and a second modulation from the scan geometry. Since this analysis focuses on a monostatic approach where $D_q(\theta) = D_q(\varphi)$, equation 3.2 takes the form:

$$s(\omega,\theta) = \sum_{q=1}^{T} \gamma_q(\theta,\varphi) F(\omega) \exp\left(-2jkD_q(\theta)\right) \tag{3.2b}$$

The SPF is band limited, and in the range domain, this limit is related to the bandwidth. For the cross-range case, the scan region dictates the band limit, and this is also known as the support band. In section 2.3 it is shown that the point spread function (PSF) for the range domain is related to the bandwidth by the equality $\Delta x = \frac{c}{2B}$. Along the scan trajectory, the PSF main lobe can be approximated by $\mathrm{sinc}(\Theta_q/2\pi)$ where Θ_q is the number of samples collected for the q^{th} target. The instantaneous frequency (IF) of the SPF can be used to obtain the value Θ_q [34]. To obtain the instantaneous frequency, the change rate of the frequency angle function given by $-2jkD_q(\theta)$ or $-2jk\sqrt{R^2 + r_q^2 - 2Rr_q\cos(\phi_q - \theta_j)}$, is used. The IF of equation 3.2b is:

$$\frac{d\left(-2jkD_q(\theta)\right)}{d\theta} = \frac{2*k*R*r_q \sin(\phi_q - \theta_j)}{\sqrt{R^2 + r_q^2 - 2Rr_q\cos(\phi_q - \theta_j)}}. \tag{3.3}$$

Since *R* and r_q stay constant across all the scan positions (j), there is no phase variation in the range direction. The maximum values of the IF for equation 3.3 are given when $\phi_q - \theta_j = \pi/2$, using this value in 3.3:

$$\left.\frac{d\left(s(\omega,\theta)\right)}{d\theta}\right|_{\phi_q - \theta_j = \frac{\pi}{2}; k = k_{max}} = \frac{2k_{max}R * r_q}{\sqrt{R^2 + r_q^2}}$$

$$\left.\frac{d\left(s(\omega,\theta)\right)}{d\theta}\right|_{\phi_q - \theta_j = -\frac{\pi}{2}; k = k_{max}} = \frac{-2k_{max}Rr_q}{\sqrt{R^2 + r_q^2}}. \tag{3.4}$$

The space between each scan location has to satisfy the Nyquist-Shannon criterion, following expression 3.4:

$$\Delta\theta \leq \frac{\pi\sqrt{R^2+r_q^2}}{2k_{max}Rr_q} \rightarrow \Delta\theta \leq \frac{\lambda_{min}\sqrt{R^2+r_q^2}}{4Rr_q}, \tag{3.5}$$

where λ_{min} is the minimum wavelength of the signal used. Following equation 3.5, the minimum number of samples needed to avoid aliasing is $2\pi/\Delta\theta$. The signal analysis presented in this section is only valid if the antenna being used covers the full ROI. Otherwise the limiting factor of the number of scan positions is related to the angle of the beamwidth of the antenna, instead of the radius of the ROI.

3.3 Experimental results

To test equation 3.5, similar experiments to those in section 2.3.6.2 were carried out. Figure 2-16 shows the setup of the experiment with an ROI that has a radius of 7.5 cm. For this benchtop system equation, 3.5 shows a minimum angle between scan locations of 10.6 degrees, for a total to 34 scan locations in air. When oil is used as a coupling medium, the minimum wavelength decreases, and 48 steps are needed.

For this experiment a scan with 144 locations was taken, then the datasets were down-sampled by different factors to get a dataset with fewer scan locations. The position of the targets was measured and compared to the phantom.

Tables 3-1, 3-2, 3-3 and 3-4 show the results of the different experiments carried out. For the experiments where there is no tumor, the TFR is not available. While the number of measurements was as low as nine steps (scan positions), not all images were possible to analyze as, below 16 scan

locations some images did not offer useful information. The location error increased as the number of steps was reduced. With a small number of scan locations, the noise is significant, and the location error is too large to detect the response from the targets reliably.

There is a correlation between the SNR, SCR, TFR, and spatial error and the number of scan locations. This correlation is present in most of the results, with some exceptions. When there is no tumor present in the phantom, the SNR and SCR are more stable. This is also true for location L where the tumor is behind a fibroglandular target. In this case, the results follow the same pattern as Section 2.3.6.2 where the Horn antenna had better TFR but worse SNR. The SCR, TFR and spatial error are less reliable to measure the drop in quality when reducing the number of scan locations.

For the experiments taken in air there, is a drop in SNR when the number of steps goes from 36 to 24. This is congruent with the 34 scan locations calculated from formula 3.5. The decline in quality is more prominent in the SNR than in the other metrics. Figure 3-2 and Figure 3-3 show the SNR for the experiments in air. For the horn antenna in air, the SNR drop is more prominent when the tumor is at position R (facing the antennas) and less prominent when there is no tumor. This decrease in SNR is at least 1 dB when going from 36 to 24 steps, and higher when comparing 36 to 18 steps. This can be compared to the drop between 48 and 36 scan locations, where the change in SNR is less than 1 dB.

The oil experiments follow a similar pattern as the air experiments. This is an interesting result since equation 3.5 predicts a need for 48 scan locations. Equation 3.5 shows that the minimum number of steps is related to the minimum wavelength of the signal used. When the antennas are submerged in oil, the minimum wavelength increases. For the cross-range resolution, the

wavelength is important since it helps to separate two targets that may have a similar distance $D_q(\theta)$ from the antenna.

3.4 Discussion

The analysis presented in Section 3.2 is based on the signal model of the microwave imaging system. While this analysis is a good approximation, the results in oil show that the minimum wavelength may not affect the reconstruction as much as predicted. In Section 2.3.1 it was shown that the range resolution depends on the bandwidth of the system and the speed of the wave. A future analysis may be improved by taking the bandwidth into account. A second explanation of the results comes from our simple phantom. The two targets used are separated by 6.3 cm, which is too large to test the resolution capabilities of the system.

The experimental results may not push the resolution of the system, but they do show the benefit of a higher number of scan locations. Above 24 positions the TFR, SNR, and SCR are higher and more stable, and the location error is less pronounced. The shift of the spatial error is evident in Figure 3-6 and Figure 3-7 where the targets slowly migrate farther away from the initial position. More steps also have the advantage of giving a higher power overall.

One of the most challenging features to measure in the image is how well defined the targets are. The fibroglandular patches are roughly spherical (as well as the tumor). An ideal reconstruction would yield a circular target of 1.5 cm diameter. In the results presented, the targets have an oval shape in the reconstructed image in air. This shape becomes more pronounced as the number of scan locations is reduced. Figure 3-6 shows how the targets have a higher eccentricity as the number of steps is reduced. When oil is used (Figure 3-7) the shape of the targets is changing too.

At 72 scan locations the targets may form a crude circle, and as the number of steps is reduced, the targets lose their circular shape.

Choosing the number of scan locations is a challenge. While a greater number of steps would record more information, it would also mean a longer scan time (or a larger number of antennas). The analysis of Section 3.2 gives a good approximation for the number of scan locations for different situations. The experimental results of section 3.3 show that the SNR, SCR, and TFR do not improve significantly beyond 36 scan locations. These results give a good starting point for determining the number of scan locations needed for the volunteer trials.

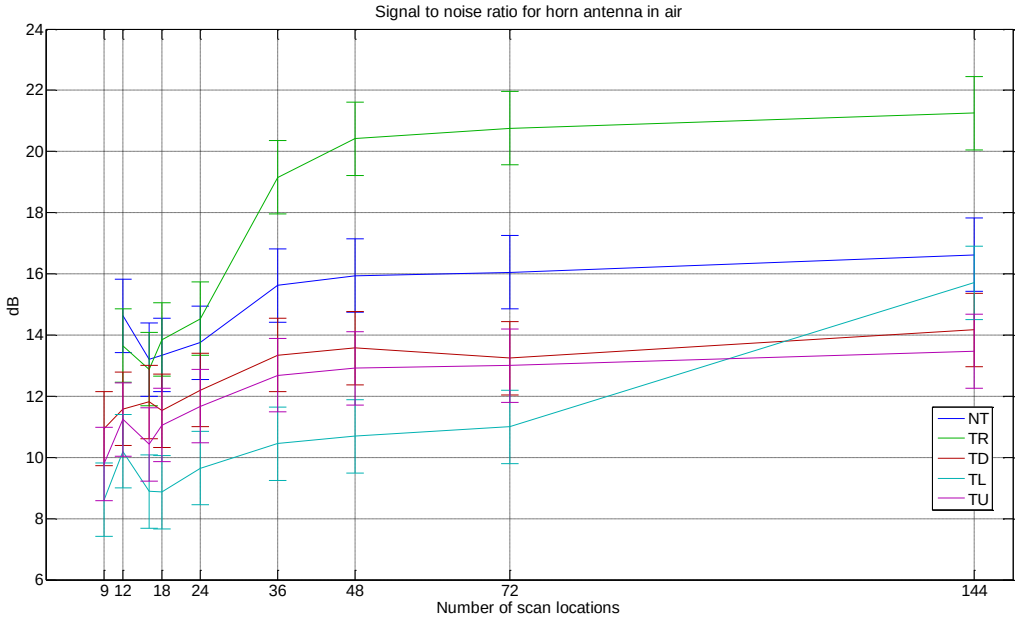

Figure 3-2 Graph showing the SNR as the number of scan locations is reduced for horn antenna in air. Bellow 36 steps the SNR drops an average of 1 dB. When there is no tumor present, the drop in SNR is not as prominent. NT=no tumor, TR = Tumor at R position (closest to antenna), TD= tumor at D position (side of fibroglandular patch), TL= tumor at L position (behind fibroglandular target), TU = tumor at U position (side of fibroglandular patch)

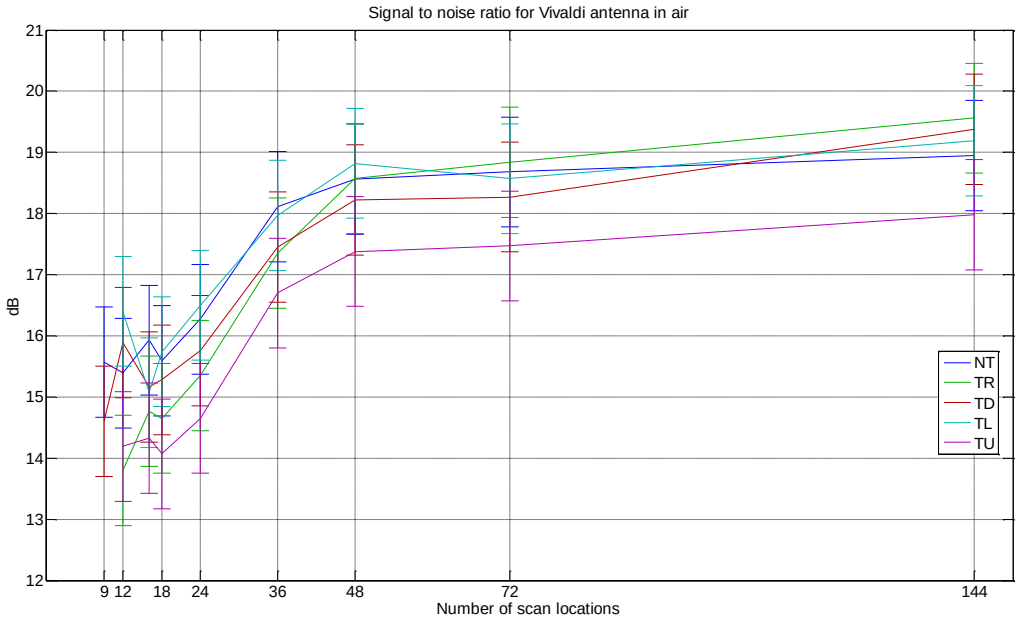

Figure 3-3 Graph showing the SNR as the number of scan locations is reduced for Vivaldi antenna in air. Bellow 36 steps the SNR drops by almost 2 dB. The Vivaldi antenna shows a more pronounced change after the 36 scan locations when compared to the horn antenna. NT=no tumor, TR = Tumor at R position (closest to antenna), TD= tumor at D position (side of fibroglandular patch), TL= tumor at L position (behind fibroglandular target), TU = tumor at U position (side of fibroglandular patch)

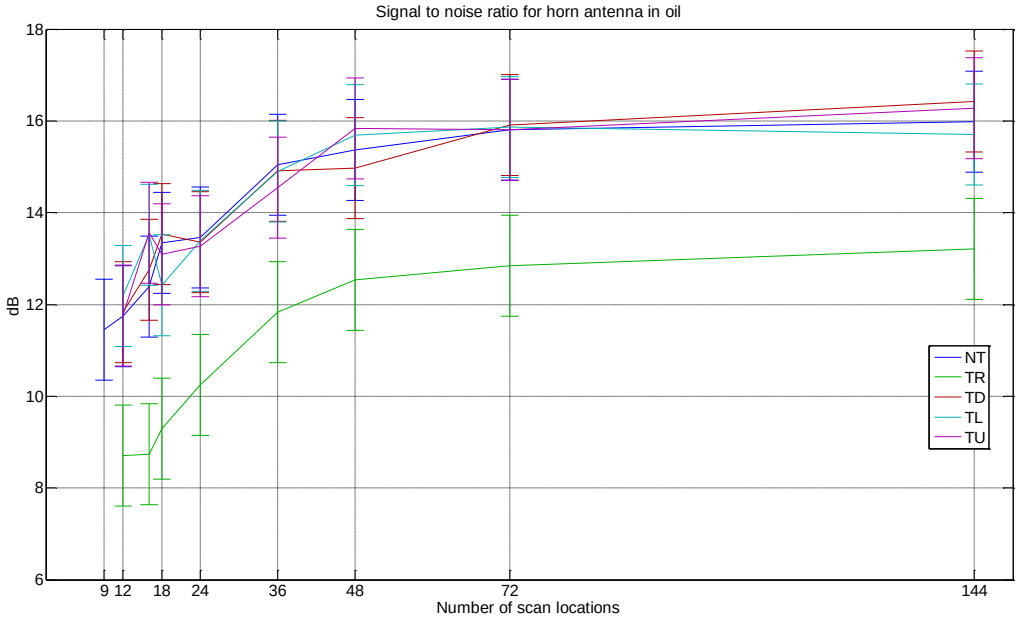

Figure 3-4 Graph showing the SNR as the number of scan locations is reduced for horn antenna in oil. Bellow 36 steps the SNR drops by an average of 1.5 dB. This is at odds with the number of steps required by equation 3.5. For this case there was a recalibration after the tumor in position R was taken, giving it a better SNR to the other four measurements. NT=no tumor, TR = Tumor at R position (closest to the antenna), TD= tumor at D position (the side of fibroglandular patch), TL= tumor at L position (behind the fibroglandular target), TU = tumor at U position (the side of fibroglandular patch)

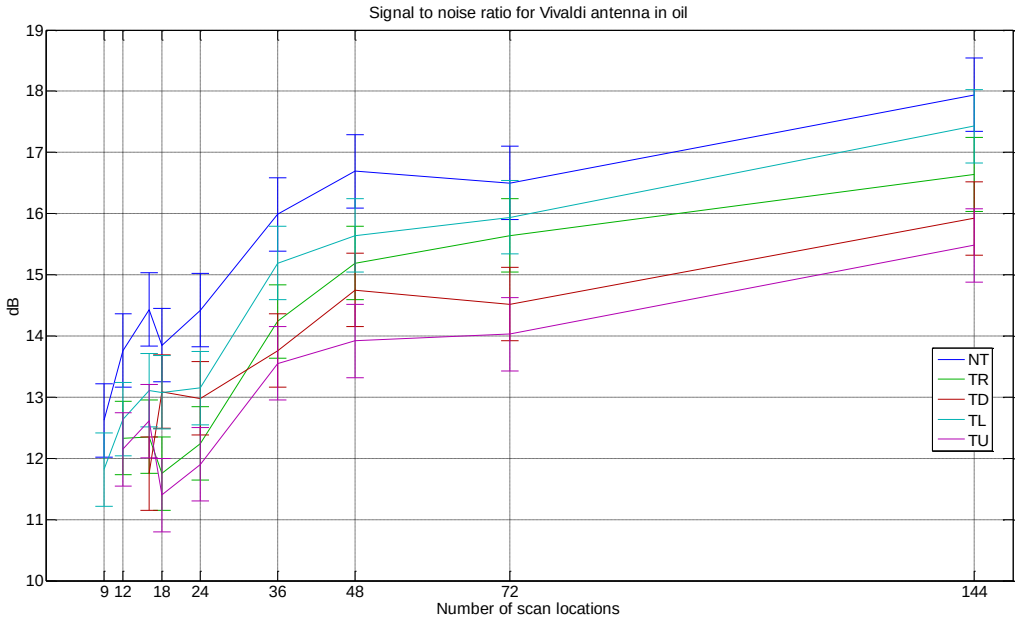

Figure 3-5 Graph showing the SNR as the number of scan locations is reduced for Vivaldi antenna in oil. Bellow 36 steps the SNR drops by 2 dB. This is at odds with the number of steps required by equation 3.5. NT=no tumor, TR = Tumor at R position (closest to antenna), TD= tumor at D position (side of fibroglandular patch), TL= tumor at L position (behind fibroglandular target), TU = tumor at U position (side of fibroglandular patch)

Horn antenna, no tumor present					Horn antenna, Tumor at R position				
Steps	SNR (dB) (±1.2)	SCR (dB) (±0.4)	TFR (dB) (±0.4)	Error (m.) (± 0.004 m)	Steps	SNR (dB) (±1.2)	SCR (dB) (±0.4)	TFR (dB) (±0.4)	Error (m.) (± 0.004 m)
144	16.6	5.0	NA	0.020	144	21.3	13.1	21.7	0.028
72	16.1	4.8	NA	0.020	72	20.8	13.6	20.4	0.028
48	15.9	4.9	NA	0.010	48	20.4	13.0	19.6	0.028
36	15.6	4.8	NA	0.010	36	19.2	13.0	18.5	0.028
24	13.8	4.9	NA	0.010	24	14.5	9.8	17.8	0.028
18	13.3	4.9	NA	0.020	18	13.9	7.3	14.9	0.028
16	13.2	4.8	NA	0.020	16	12.9	7.4	NA	0.033
12	14.6	4.9	NA	0.050	12	13.7	4.7	NA	0.028
9	NA	NA	NA	NA	9	NA	NA	NA	NA

Horn antenna, Tumor at D position					Horn antenna, Tumor at L position				
Steps	SNR (dB) (±1.2)	SCR (dB) (±0.4)	TFR (dB) (±0.4)	Error (m.) (± 0.004 m)	Steps	SNR (dB) (±1.2)	SCR (dB) (±0.4)	TFR (dB) (±0.4)	Error (m.) (± 0.004 m)
144	14.2	9.2	11.6	0.033	144	15.7	7.2	8.8	0.028
72	13.2	8.5	9.9	0.033	72	11.0	4.8	3.4	0.028
48	13.6	7.1	9.4	0.033	48	10.7	4.8	2.3	0.028
36	13.3	7.1	9.7	0.033	36	10.4	5.1	1.4	0.028
24	12.2	7.0	8.1	0.043	24	9.6	3.2	0.5	0.028
18	11.5	6.1	6.8	0.053	18	8.9	3.3	-1.2	0.048
16	11.8	4.8	5.4	0.053	16	8.9	3.2	-2.6	0.048
12	11.6	4.8	3.2	0.053	12	10.2	3.0	-1.2	0.068
9	10.9	3.3	0.5	0.063	9	8.6	1.8	-0.3	0.048

Horn antenna, Tumor at U position				
Steps	SNR (dB) (±1.2)	SCR (dB) (±0.4)	TFR (dB) (±0.4)	Error (m.) (± 0.004 m)
144	13.5	9.1	14.2	0.018
72	13.0	7.2	12.5	0.028
48	12.9	7.0	10.9	0.023
36	12.7	7.3	10.5	0.023
24	11.7	7.0	10.4	0.023
18	11.1	6.7	11.1	0.013
16	10.4	5.8	9.3	0.043
12	11.2	4.8	8.5	0.023
9	9.8	3.4	10.2	0.063

Table 3-1 Results of the experiments performed with the Horn antenna in air with a glycerin phantom. As the number of steps (scan positions) is reduced, the SNR decreases and the error gets bigger. The error is measured against the position in the phantoms, and it is a sum of the error of both targets.

Vivaldi antenna, no tumor present.					Vivaldi antenna, Tumor at R position				
Steps	SNR (dB) (±0.9)	SCR (dB) (±0.6)	TFR (dB) (±0.6)	Error (m.) (± 0.004 m)	Steps	SNR (dB) (±0.9)	SCR (dB) (±0.6)	TFR (dB) (±0.6)	Error (m.) (± 0.004 m)
144	19.0	7.1	NA	0.020	144	19.6	7.7	10.8	0.018
72	18.7	6.4	NA	0.020	72	18.8	7.2	9.0	0.018
48	18.6	6.3	NA	0.020	48	18.6	7.0	8.2	0.028
36	18.1	6.6	NA	0.020	36	17.4	4.9	5.7	0.028
24	16.3	6.4	NA	0.020	24	15.3	5.0	6.0	0.018
18	15.6	6.3	NA	0.020	18	14.6	4.7	3.5	0.018
16	15.9	6.0	NA	0.030	16	14.8	4.4	1.3	0.018
12	15.4	6.1	NA	0.040	12	13.8	2.2	-0.5	0.053
9	15.6	3.3	NA	0.060	9	NA	NA	NA	NA

Vivaldi antenna, Tumor at D position					Vivaldi antenna, Tumor at L position				
Steps	SNR (dB) (±0.9)	SCR (dB) (±0.6)	TFR (dB) (±0.6)	Error (m.) (± 0.004 m)	Steps	SNR (dB) (±0.9)	SCR (dB) (±0.6)	TFR (dB) (±0.6)	Error (m.) (± 0.004 m)
144	19.4	7.1	-0.4	0.013	144	19.2	7.0	-8.4	0.038
72	18.3	5.0	-0.7	0.013	72	18.6	7.0	-9.3	0.038
48	18.2	4.9	-1.7	0.023	48	18.8	7.2	-8.7	0.048
36	17.5	4.8	-1.9	0.023	36	18.0	7.1	-9.0	0.048
24	15.8	5.1	-5.5	0.023	24	16.5	7.7	-10.9	0.038
18	15.3	5.5	-3.7	0.028	18	15.7	7.0	-11.7	0.038
16	15.2	4.8	-4.3	0.028	16	15.1	7.0	-11.4	0.038
12	15.9	4.9	-6.1	0.038	12	16.4	7.3	-8.0	0.068
9	14.6	4.8	-4.4	0.038	9	NA	NA	NA	NA

Vivaldi antenna, Tumor at U position				
Steps	SNR (dB) (±0.9)	SCR (dB) (±0.6)	TFR (dB) (±0.6)	Error (m.) (± 0.004 m)
144	18.0	7.1	2.9	0.018
72	17.5	7.8	1.4	0.018
48	17.4	7.1	2.5	0.018
36	16.7	7.6	2.9	0.028
24	14.7	7.0	2.5	0.028
18	14.1	7.0	0.7	0.028
16	14.3	7.1	-0.9	0.023
12	14.2	7.3	2.5	0.028
9	NA	NA	NA	NA

Table 3-2 Results of the experiments performed with the Vivaldi antenna in air with a glycerin phantom. As the number of steps (scan positions) is reduced, the SNR decreases and the error gets bigger. The error is measured against the position in the phantoms, and it is a sum of the error of both targets.

Horn antenna in oil, no tumor present.					Horn antenna in oil, Tumor at R position				
Steps	SNR (dB) (±1.1)	SCR (dB) (±0.5)	TFR (dB) (±0.5)	Error (m.) (± 0.005 m)	Steps	SNR (dB) (±1.1)	SCR (dB) (±0.5)	TFR (dB) (±0.5)	Error (m.) (± 0.005 m)
144	16.0	7.1	NA	0.036	144	13.2	4.8	3.6	0.026
72	15.8	6.6	NA	0.029	72	12.8	4.1	4.6	0.019
48	15.4	6.7	NA	0.036	48	12.5	4.4	4.1	0.026
36	15.0	7.0	NA	0.043	36	11.8	4.5	3.8	0.033
24	13.5	6.6	NA	0.043	24	10.2	4.1	0.8	0.033
18	13.3	6.7	NA	0.049	18	9.3	1.7	2.8	0.033
16	12.4	6.7	NA	0.049	16	8.7	1.8	1.5	0.060
12	11.7	4.1	NA	0.056	12	8.7	0.7	2.7	0.060
9	11.4	3.9	NA	0.063	9	NA	NA	NA	NA

Horn antenna in oil, Tumor at D position					Horn antenna in oil, Tumor at L position				
Steps	SNR (dB) (±1.1)	SCR (dB) (±0.5)	TFR (dB) (±0.5)	Error (m.) (± 0.005 m)	Steps	SNR (dB) (±1.1)	SCR (dB) (±0.5)	TFR (dB) (±0.5)	Error (m.) (± 0.005 m)
144	16.4	7.2	11.5	0.040	144	15.7	7.2	10.9	0.031
72	15.9	6.2	11.4	0.040	72	15.9	7.3	10.9	0.038
48	15.0	6.6	9.7	0.053	48	15.7	7.0	11.6	0.051
36	14.9	7.3	9.4	0.060	36	14.9	7.3	10.3	0.051
24	13.4	5.7	7.4	0.067	24	13.4	9.2	12.1	0.058
18	13.5	7.0	11.7	0.067	18	12.4	6.9	7.2	0.058
16	12.8	5.1	8.3	0.067	16	13.5	5.0	11.1	0.056
12	11.8	3.8	8.4	0.067	12	12.2	3.6	9.7	0.045
9	NA	NA	NA	NA	9	NA	NA	NA	NA

Horn antenna in oil, Tumor at U position				
Steps	SNR (dB) (±1.1)	SCR (dB) (±0.5)	TFR (dB) (±0.5)	Error (m.) (± 0.005 m)
144	16.3	7.3	9.5	0.031
72	15.8	6.2	5.2	0.024
48	15.8	6.1	4.8	0.031
36	14.5	6.3	5.7	0.018
24	13.3	6.2	6.0	0.032
18	13.1	6.1	5.7	0.039
16	13.6	6.1	3.7	0.025
12	11.8	4.9	6.6	0.052
9	NA	NA	NA	NA

Table 3-3 Results of the experiments performed with the Horn antenna in oil with a glycerin phantom. As the number of steps (scan positions) is reduced, the SNR decreases and the error gets bigger. The error is measured against the position in the phantoms, and it is a sum of the error of both targets.

Vivaldi antenna in oil, no tumor present.					Vivaldi antenna in oil, Tumor at R position				
Steps	SNR (dB) (±0.6)	SCR (dB) (±0.4)	TFR (dB) (±0.4)	Error (m.) (± 0.005 m)	Steps	SNR (dB) (±0.6)	SCR (dB) (±0.4)	TFR (dB) (±0.4)	Error (m.) (± 0.005 m)
144	17.9	5.6	NA	0.039	144	16.6	5.2	3.4	0.026
72	16.5	5.1	NA	0.047	72	15.6	4.8	2.0	0.035
48	16.7	4.8	NA	0.039	48	15.2	4.9	3.4	0.026
36	16.0	4.8	NA	0.030	36	14.2	4.4	4.5	0.026
24	14.4	5.3	NA	0.030	24	12.2	2.8	-0.8	0.026
18	13.9	5.1	NA	0.030	18	11.8	2.8	-3.0	0.013
16	14.4	5.1	NA	0.030	16	12.4	3.3	-0.4	0.018
12	13.8	5.0	NA	0.047	12	12.3	1.7	1.9	0.039
9	12.6	2.2	NA	0.056	9	NA	NA	NA	NA

Vivaldi antenna in oil, Tumor at D position					Vivaldi antenna in oil, Tumor at L position				
Steps	SNR (dB) (±0.6)	SCR (dB) (±0.4)	TFR (dB) (±0.4)	Error (m.) (± 0.005 m)	Steps	SNR (dB) (±0.6)	SCR (dB) (±0.4)	TFR (dB) (±0.4)	Error (m.) (± 0.005 m)
144	15.9	3.5	-5.2	0.034	144	17.4	5.0	1.3	0.056
72	14.5	2.3	-5.0	0.034	72	15.9	4.7	2.6	0.056
48	14.7	2.3	-5.4	0.034	48	15.6	3.9	1.5	0.056
36	13.8	1.7	-3.9	0.025	36	15.2	3.5	0.7	0.056
24	13.0	1.6	-5.3	0.017	24	13.2	3.3	1.0	0.039
18	13.1	1.7	-5.9	0.021	18	13.1	3.2	1.0	0.035
16	11.8	0.5	-4.9	0.018	16	13.1	3.4	1.2	0.043
12	NA	NA	NA	NA	12	12.6	3.4	-1.4	0.056
9	NA	NA	NA	NA	9	11.8	1.1	-1.3	0.056

Vivaldi antenna in oil, Tumor at U position				
Steps	SNR (dB) (±0.6)	SCR (dB) (±0.4)	TFR (dB) (±0.4)	Error (m.) (± 0.005 m)
144	15.5	4.7	0.9	0.065
72	14.0	4.3	0.9	0.065
48	13.9	4.4	0.7	0.056
36	13.6	4.3	1.4	0.056
24	11.9	3.4	0.4	0.048
18	11.4	2.4	0.1	0.048
16	12.6	3.6	-1.4	0.048
12	12.1	2.5	0.7	0.073
9	NA	NA	NA	NA

Table 3-4 Results of the experiments performed with the Vivaldi antenna in oil with a glycerin phantom. As the number of steps (scan positions) is reduced, the SNR decreases and the error gets bigger. The error is measured against the position in the phantoms, and it is a sum of the error of both targets.

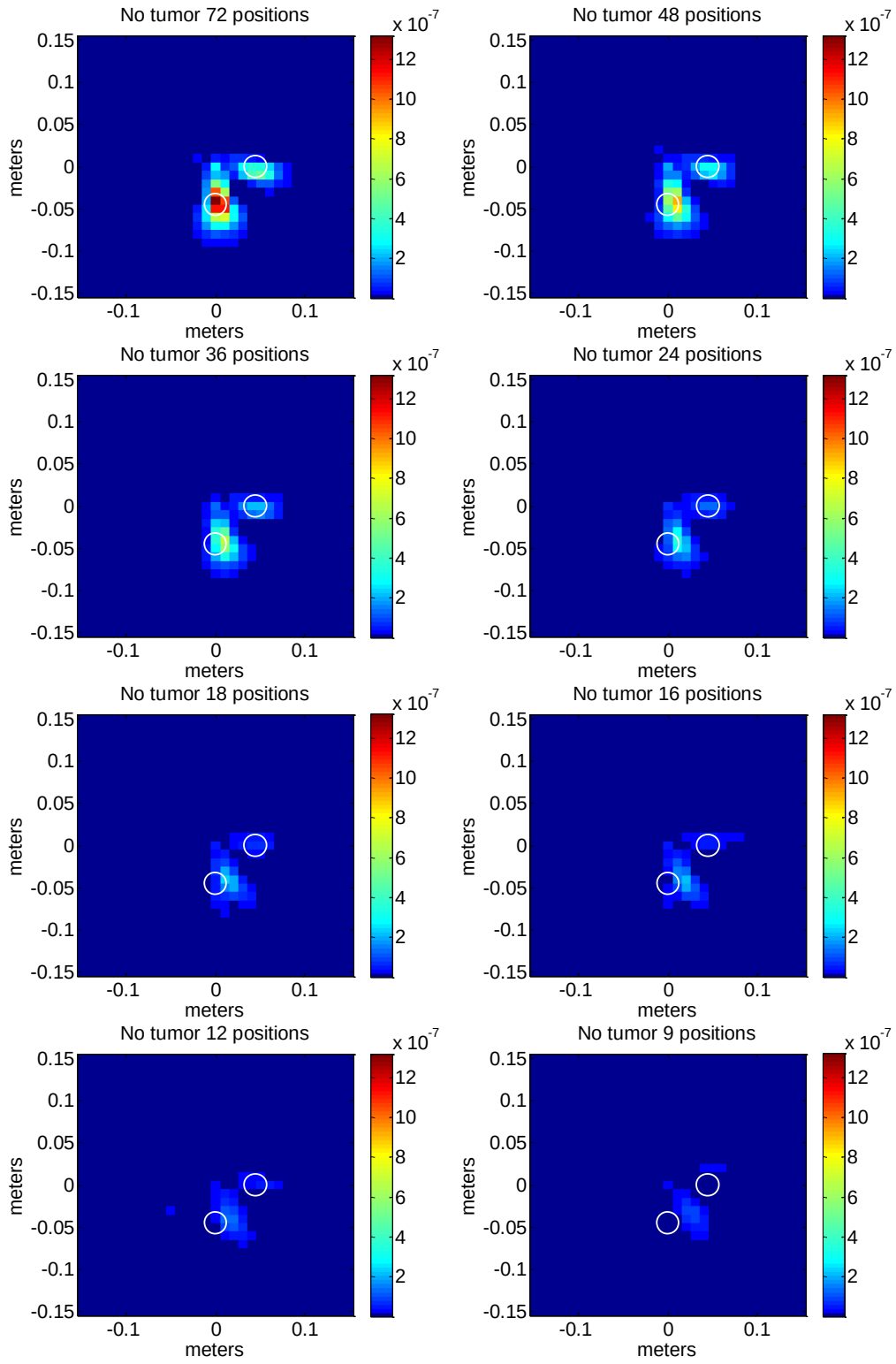

Figure 3-6 Experimental results with different numbers of scan positions for a Vivaldi antenna in air, using the setup shown in figure 2-16. The figure with 144 steps is omitted since there is a high similitude with the 72 steps reconstruction. As the number of scan positions decreases the targets shift from the expected position.

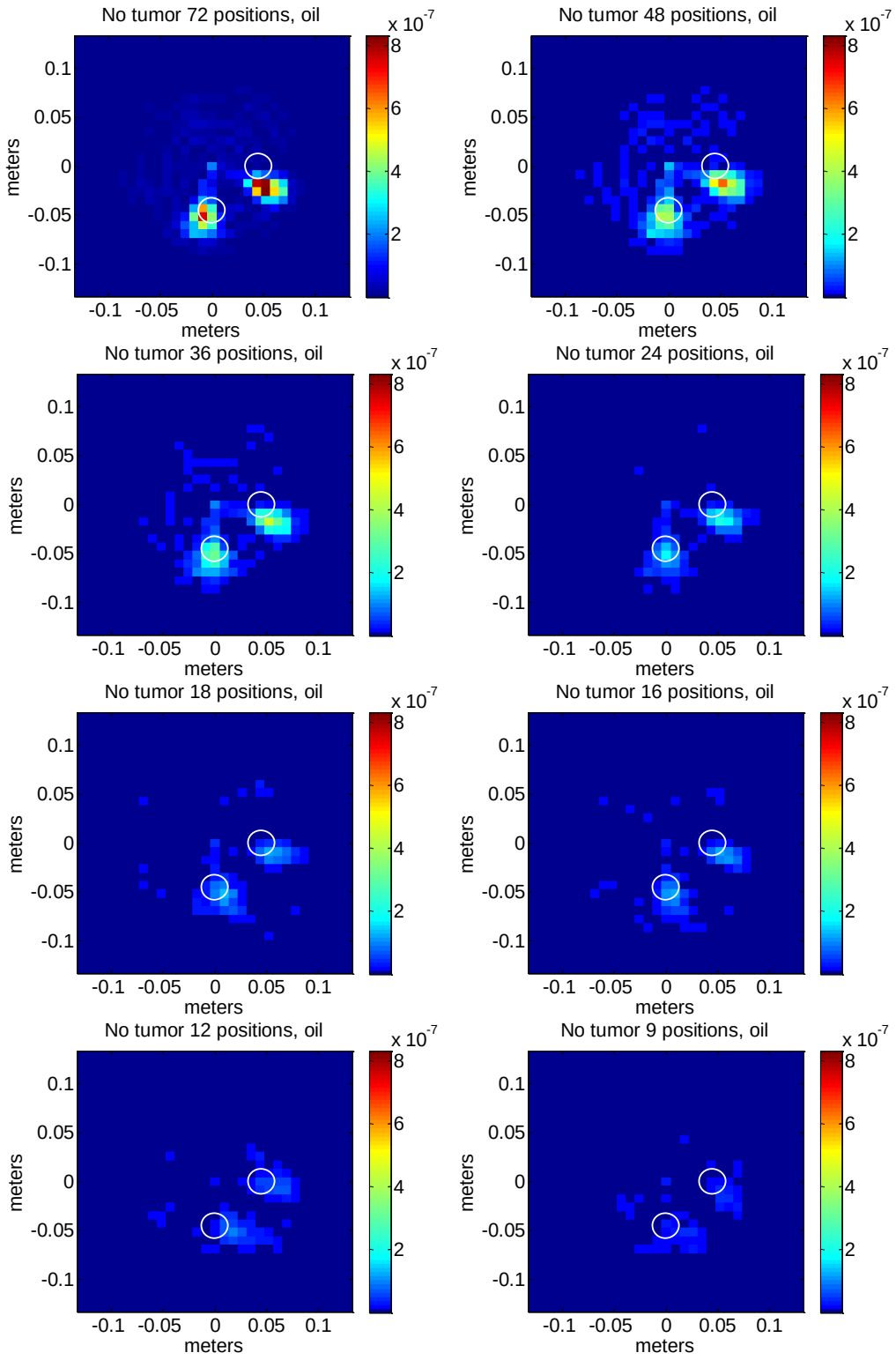

Figure 3-7 Experimental results with different numbers of scan positions for a Vivaldi antenna in oil, using the setup shown in figure 2-16. The figure with 144 steps is omitted since there is a high similitude with the 72 steps reconstruction. As the number of scan positions decreases the targets shift from the expected position

4 Wave speed estimation in breast microwave imaging scenarios using image quality metrics

This chapter contains material that has been reprinted and adapted from a conference proceeding: Rodriguez-Herrera, D., Flores-Tapia, D. and Pistorius, S., 2014, April. Comparison of image quality metrics for electromagnetic wave propagation speed estimation in Breast Microwave Radar imaging scenarios. In Antennas and Propagation (EuCAP), 2014 8th European Conference on (pp. 516-519). Copyright © 2014 IEEE.

4.1 Background and problem definition

The reconstruction algorithm used in this work is based on a circular holography algorithm described in Section 1.3.4.2. The reconstruction uses a matched filter $M_f(\omega, c_n, \varphi)$ (given by 4.1) to compensate for a circular scan trajectory. The inputs of the filter are K=ω/c_n (the wave number), and ϕ is the frequency representation of the cross-range domain.

$$M_f(\omega, c_n, \varphi) = e^{-j\left(\sqrt{4(\omega/c_n)^2R^2-\varphi^2}+\varphi \sin^{-1}\left(\frac{\varphi}{2(\omega/c_n)}\right)+\varphi\pi\right)}, \quad (4.1)$$

R is a fixed value since the radius is determined by the scan geometry and the signal delay from the antenna (see Chapter 2 for the signal delay in the antennas used). φ is the Fourier transform of the obtained datasets in the slow-time domain. The angular frequency (ω) depends on the bandwidth used in the system.

The only unknown parameter from Eq. 4.1 is the speed of the wave in the medium (c_n). The c_n parameter is determined by the dielectric properties of the medium. In case of breast tissue different studies have reported the permittivity and conductivity by measuring after or during a surgery [7, 11]. However, these results present some inconsistency since doing in-vivo measurements is challenging due to the risk for the volunteer. Even if all the dielectric properties of the tissues are known every woman has a unique combination of fatty tissue and fibroglandular tissue. The composition of the breast changes between patients and it also changes as the person

ages. These constraints make it difficult to have an estimation of the speed of the wave inside the breast.

A reliable way to estimate the propagation speed inside the breast allows for a more robust system than can be used in human subjects. In a benchtop system, all dielectric properties of materials used are known, but this is not the case in a clinical environment.

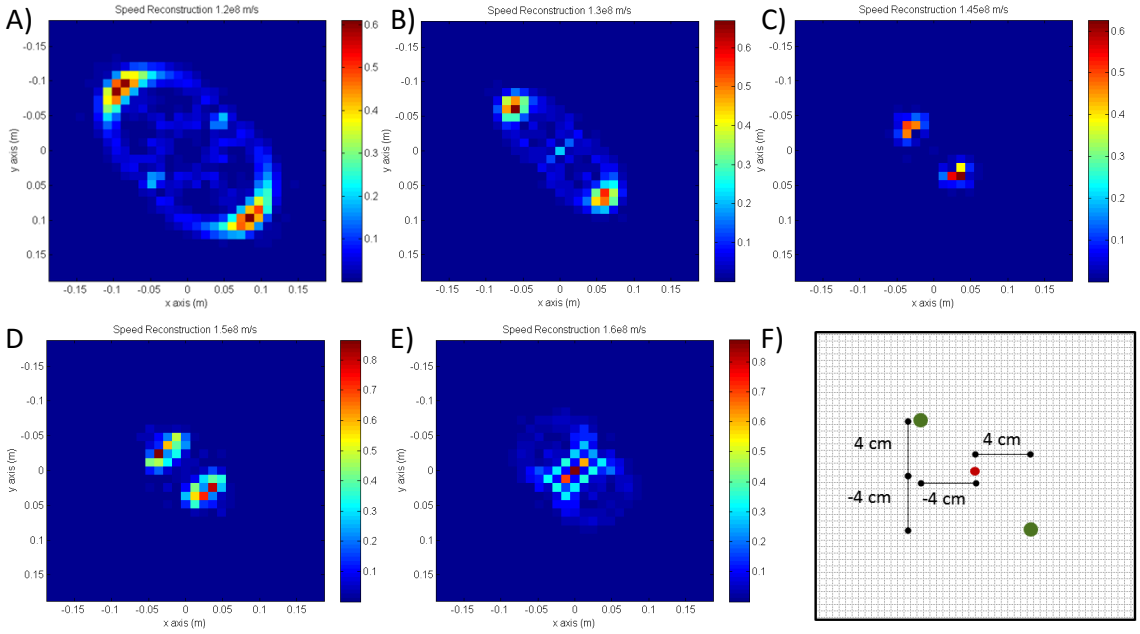

Figure 4-1 A simulated set up shows how the input parameter c_n affects the reconstruction. F) Shows the simulated set up with two targets, C) shows the reconstruction of the targets using the correct speed (1.45 x10^8 m/s). A) And B) show how underestimating the speed shifts the targets away from the center. A) Is the reconstruction at 1.2x10^8 m/s. B) shows the reconstruction at 1.3x10^8 m/s. D) and E) show an overestimation of the speed, in this case the targets shift to the center of the image. D) Uses a speed of 1.5 x10^8 m/s and E) uses 1.6 x10^8 m/s

To demonstrate the effect of c_n in the reconstruction, a dataset was simulated, with two targets inside a medium where the speed is 1.45x10^8 m/s (Figure 4-1). For this simulation, the targets have a point-like structure. When the correct speed is used, the targets are accurately positioned in the resulting image. An underestimation of the speed shifts the targets away from the center of the image and the PSF of the system widens creating bigger targets. When the speed is overestimated, the targets shift to the center of the image.

In this chapter, a method of wave speed estimation base on image quality metrics is presented. Section 4.2 presents objective image quality metrics that do not depend on knowledge of the ROI. Section 4.3 shows the result of the image quality metrics when evaluated in simulated datasets. Sections 4.4, 4.5 and 4.6 provide the methodology and result of experimental datasets to test the image quality metrics.

4.2 Image quality metrics

Independent, objective image metrics are metrics that do not require human input or previous knowledge of the scan region. In Section 2.2.5.1, image quality metrics that require previous knowledge of the ROI were presented. These metrics are useful to compare images of the same phantom taken under different circumstances (different VNA, antennas, etc.). These metrics are not useful for patient imaging since there is no knowledge of the breast configuration. Objective images allow us to compare images even when the ROI is not known, making them useful to compare images of scanned patients. Five different imaging metrics are presented in the current section. [35-40]

Entropy measures the smoothness of a distribution function. Entropy in information theory measures the distribution of data for different proposes (compression, security, etc.). In this case, the entropy is used to gauge the evenness of the histogram of a given image. A flat image would have an uneven histogram (where one value is overrepresented, and all other values are missing). An image consisting of white noise will have a smooth histogram where every value is present the same number of times. The entropy is defined as [36]

$$E = -\sum_{k=1}^{T_{val}} P_k \log_2(P_k), \tag{4.2}$$

where P is the histogram of the reconstructed image and P_k is the number of times a given value is repeated in the image. T_{val} is the total number of values in the histogram and E is a dimensionless entropy value.

To calculate the entropy, the images are converted to grayscale, the maximum value of the image is set as 1 (White) and the minimum value as 0 (black). The resulting image is a 64-bit grayscale image where $T_{val} = 2^{64}$. This is done to normalize the set of values used across different images where the maximum and minimum value may differ drastically.

The contrast of an image measures the difference between the brightest and the dimmest area of an image. A general definition of contrast measures the maximum amplitude of an image $\max(I(m,n))$ however this definition is only useful for very simple applications where only one target is present. The sum of image intensity performs better [41].

$$C = \frac{\sum_{m=1}^{M}\sum_{n=1}^{N}[I(m,n)]^2}{\left[\sum_{m=1}^{M}\sum_{n=1}^{N} I(m,n)\right]^2} \tag{4.2}$$

Gradient metrics measure the sharpness of an image by measuring the change rate between adjacent pixels. The Sobel (S_x, S_y) and Laplace (L) filters are used to calculate the image gradient. These two filters are normally used for edge detection algorithms. The filters are defined as follows [38]

$$S_x = \frac{1}{4}\begin{Bmatrix} -1 & 0 & 1 \\ -2 & 0 & 2 \\ -1 & 0 & 2 \end{Bmatrix} \quad S_y = \frac{1}{4}\begin{Bmatrix} 1 & 2 & 1 \\ 0 & 0 & 0 \\ -1 & -2 & -1 \end{Bmatrix}; L = \frac{1}{6}\begin{Bmatrix} 1 & 4 & 1 \\ 4 & -20 & 4 \\ 1 & 4 & 1 \end{Bmatrix} \tag{4.3}$$

Once the gradient is calculated using the Sobel or Laplace filters the gradient metric is defined by

$$GRAD(I) = \sum_{m=1}^{M}\sum_{n=1}^{N}[F_i(m,n)]^2 \quad for\ |F_i(m,n)| > T \tag{4.4}$$

Where F_i represents the image after the gradient filters where applied, and T is a threshold value, for focusing applications normally T=0 [38]. When the Sobel filters are used the gradient metric is known as Tenengrad, when the Laplace filter is used the metric keeps the name of the filter.

As a final metric, we are using the Variance. The Variance also measures the smoothness of the histogram.

The speed-search algorithm used in this work generates a series of reconstructed images at different equidistant speeds from $1x10^8$ m/s to $3.1x10^8$ m/s. Each dataset is reconstructed 201 times. The range of the speed search can be narrowed if there is a coupling medium.

4.3 Performance of image quality metrics in simulated datasets

To test the IQM (image quality metrics) presented, a series of datasets in different mediums was simulated. The simulation is performed in a similar manner as the technique described in [41]. Once the dataset is generated, a reconstruction is performed, and the image metrics are applied to the reconstructed image. We repeat this process for a range of speeds ($1x10^8$ m/s to $2.1x10^8$ m/s) based on the possible speeds inside a breast. Using the metrics then we can find the speed that generates the image that is best focused.

The simulations are done using a range of contrasts between medium and target of 50% to 400%. This range is consistent with the reported contrast between fatty tissue and malignant tissue [7, 11]. For the datasets in this section both the dielectric properties of the medium and the target were altered. Gaussian noise was added to half of the simulations done to test how well the metrics would perform in noisy data.

A total of eleven simulations were generated, a set of six had a fixed ε_r of 4.28 (for a wave speed of 1.45x10^8 m/s). The remaining datasets change the relative permittivity of the medium. Three tumor-like targets were used in all datasets, spread evenly around a circumference with a radius of two centimeters. A monostatic scan was used with antennas evenly distributed around the ROI, the circular geometry has a radius of 20 cm. 144 scan locations where used for all datasets (see Figure 4-2).

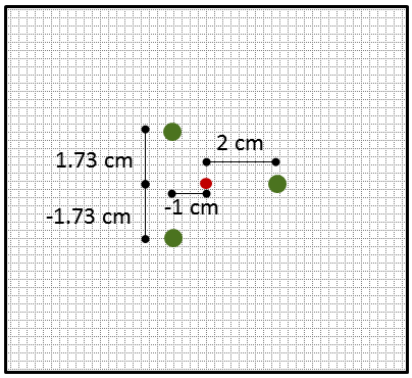

Figure 4-2 Set up for the simulated datasets. 11 datasets were generated. The contrast between target and medium is 50% to 400%. Three datasets had complex Gaussian noise added. 144 scan locations were used at a radius of 20 cm.

For this initial trial based on simulations, four IQM are tested (Contrast, Entropy, Tenengrad, Laplace). Without any noise added all metrics have a similar performance. Using the speed-search algorithm, the IQM converge to the same speed (1.43x10^8 m/s ±0.005x10^8). Figure 4-3 shows the images reconstructed using the simulated speed and the speed reported by the speed-search algorithm. The differences are small.

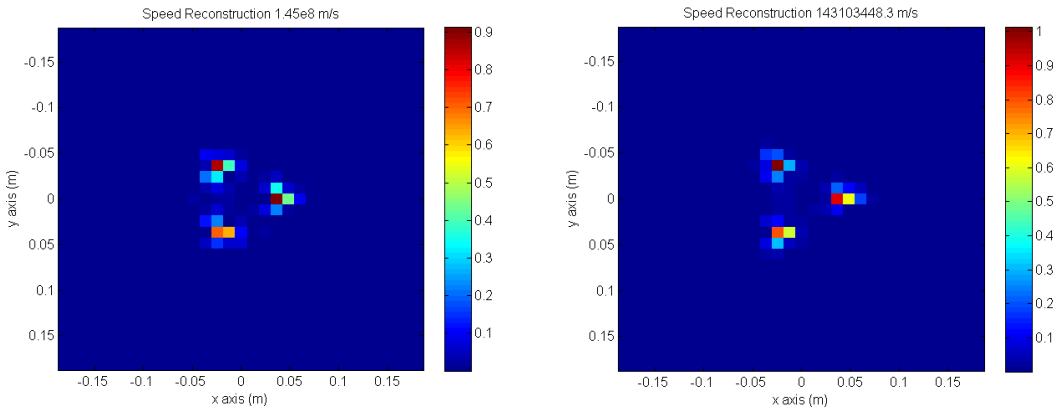

Figure 4-3 Comparison of an image reconstructed using the original simulated speed (1.45e08 m/s) and the speed estimated using the IQM. The targets are at (2, 0) cm, (-1, 1.73) cm and (-1, -1.73) cm. The images are very similar but for a small change in intensity of the targets. The figure was taken from [43] Copyright © 2014 IEEE.

The result of the speed-search algorithm is the same when the contrast of the targets and medium is changed. Three simulated datasets were tested with an ε_r of 10, 25 and 35. The IQM converge to the same speed for the three datasets. Table 4-1 shows a summary of the results.

Three new datasets were simulated with Gaussian noise added and using the same dielectric properties. The SNR of the new datasets is 1.2. When the relative permittivity is 25 or 35 all the metrics report a similar speed, but when the contrast falls to 50%, the entropy metric reports the wrong speed. Figure 4-4 shows the reconstructed images after Gaussian noise is added.

Simulations without Gaussian noise[a]				
ε_r	**Contrast**	**Entropy**	**Tenengrad**	**Laplace**
10	1.43 e+08	1.43 e+08	1.43 e+08	1.43 e+08
25	1.43 e+08	1.43 e+08	1.43 e+08	1.43 e+08
35	1.43 e+08	1.43 e+08	1.43 e+08	1.43 e+08
Simulations with added Gaussian noise[a]				
ε_r	**Contrast**	**Entropy**	**Tenengrad**	**Laplace**
10	1.46 e+08	2.10 e+08	1.46 e+08	1.40 e+08
25	1.43 e+08	1.42 e+08	1.43 e+08	1.43 e+08
35	1.44 e+08	1.44 e+08	1.44 e+08	1.44 e+08

[a]All speeds on m/s, simulated speed is 1.444x108 m/s

Table 4-1 shows a summary of the results of the simulated datasets. When there is no noise present, all the metrics get close to the target speed of 1.45x10^8 m/s. When noise was present, the entropy metric had problems when a low contrast between targets and medium was used. The table was taken from [43] Copyright © 2014 IEEE

Entropy is a metric based on the histogram of the image, the rest of IQM are based on the image matrix. This change on input data may explain why the entropy performs worse in noisy low contrast scenarios. The contrast metric relies on the difference between the brightest values and

dimmest areas, and while the added Gaussian noise may shift the values of the faintest areas in the image, the difference was still greater when the correct speed was used, and this was true as long as the SNR is above 1. Gradient-based metrics (Tenengrad and Laplace) measure the rate of change between the areas of the image. When the incorrect speed was used, the change between the targets and the background was more gradual. This holds true for the images where the noise was added (see Figure 4-4). In the case of the entropy metric, the change of the histogram hides the value of the target. Figure 4-5 shows the histogram of a reconstructed image with and without noise. When there is no noise, the histogram has a high number of low-value pixels from the background. When Gaussian noise is added, the values in the histogram from the targets were concealed.

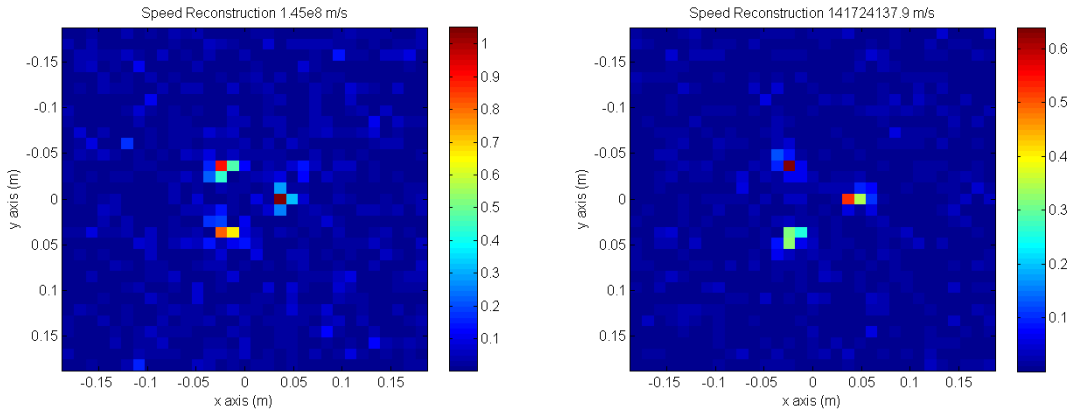

Figure 4-4 Comparison of the image with Gaussian noise. The reconstruction on the left used the original simulated speed (1.45e08 m/s) and that on the right, the speed estimated using the IQM. The targets were at (2, 0) cm, (-1, 1.73) cm and (-1, -1.73) cm. The images are very similar but for a small change in intensity of the targets. The figure was taken from [43] Copyright © 2014 IEEE.

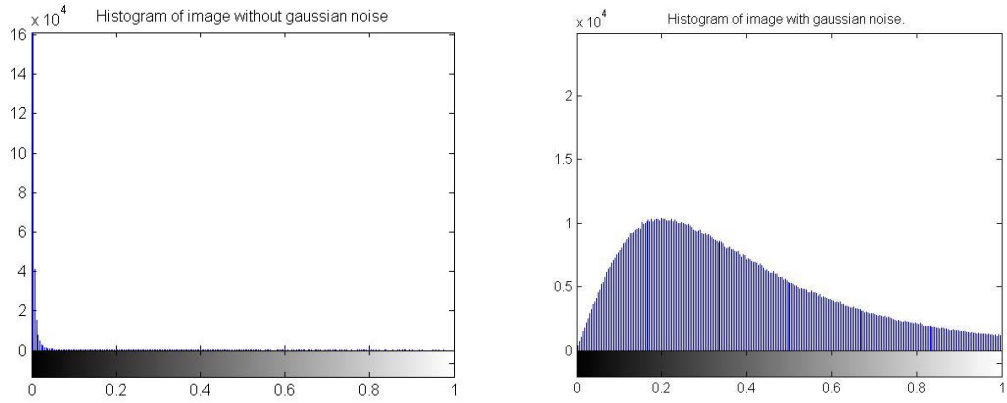

Figure 4-5 Difference between the histogram of an image with Gaussian noise and without Gaussian noise. The entropy metric uses the histogram to measure the image fitness. When Gaussian noise was added the values in the histogram from the targets were concealed, and the performance of the entropy metric dropped. The figure was taken from [43] Copyright © 2014 IEEE.

To this point, the simulations focused on changing the relative permittivity of the targets. A new set of four images were simulated where the properties of the medium were changed. The same set-up, as shown in Figure 4-2, where the targets have a $\varepsilon_r = 50$, was followed. In this case all the metrics perform well, and approximate the expected speed within ± 0.01x10^8 m/s. The results are shown in Table 4-2.

Simulated speed[b]	Contrast	Entropy	Tenengrad	Laplace
1.12 e+08	1.12 e+08	1.12 e+08	1.12 e+08	1.12 e+08
1.36 e+08	1.36 e+08	1.36 e+08	1.36 e+08	1.36 e+08
1.61 e+08	1.60 e+08	1.60 e+08	1.60 e+08	1.60 e+08
1.85 e+08	1.85 e+08	1.84 e+08	1.84 e+08	1.85 e+08

[b]All speeds on m/s, simulated speed is 1.444x108 m/s

Table 4-2 shows a summary of the results of the simulated datasets when the medium is changed. The IQM perform well. The table was taken from [43] Copyright © 2014 IEEE

The results from this initial set of simulations show that the IQM can reliably approximate the speed of the wave inside the medium. As shown in Table 4-1, when noise was added the IQM may be less reliable. The rest of this section explores the performance of the IQM when used in experimental datasets taken using phantoms.

4.4 Dielectric properties measurements.

A set of phantoms was created to test the IQM. The phantoms were created using a mixture of glycerin and water. Table 2-2 in Section 2.2.5.2 shows the relative permittivity of the materials employed in the phantoms. However, to have a greater range of contrast between medium and target a wider range of mediums is needed.

In this section, the dielectric properties of different water and glycerin mixtures are measured. The measurements were done with the Agilent 85070E dielectric probe kit from 1 to 8 GHz. Twelve measurements were performed, for canola oil, water, glycerin, and nine different mixtures of glycerin and water. Table 4-3 shows a summary of the measurements done. These measurements concur with the ones reported in the literature [44].

Material	**ε_r(1.5 GHz)**	**ε_r(4.5 GHz)**	**ε_r(7.5 GHz)**
Glycerin	9	6.6	6
90% Glycerin 10% water	11.8	7.9	7
80% Glycerin 20% water	21.2	11.3	9.2
70% Glycerin 30% water	25.8	13.1	10.4
60% Glycerin 40% water	43.5	23	16.4
50% Glycerin 50% water	52.8	32.1	22.5
Material	**ε_r(1.5 GHz)**	**ε_r(4.5 GHz)**	**ε_r(7.5 GHz)**
40% Glycerin 60% water	60.4	43	31.2
30% Glycerin 70% water	65.9	52.8	40.8
20% Glycerin 80% water	69.2	59.3	48.1
10% Glycerin 90% water	75.4	70.7	63
Water	77.5	74.5	68.5
Canola oil	2.8	2.7	2.6

Table 4-3 Dielectric properties of materials used for phantoms. The bandwidth of the system is from 1 to 8 GHz. These measurements were taken using an Agilent 85070E dielectric probe kit.

4.5 Compensation for reconstruction induced artifacts

The IQM perform very well in the simulated datasets of Section 4.2. However, the simulations make a few simplifications. The presented targets follow a delta function, and we assume the antennas are submerged in the homogenous medium of the target. Experimental datasets are more complex.

The targets may not have a uniform shape, and the antennas are not placed in the same medium as the target.

In Section 1.3.4.2, the circular holography algorithm was described, where after the matched filter is applied, a coordinate mapping is carried out. The raw data generated by the system is in the form of a square matrix. In this matrix, the range direction (columns) corresponds to the frequency data read at a given scan location. The cross-range direction (rows) corresponds to the scan positions. However, in the scan geometry, the cross-range direction follows a circular path, while the raw data shows a linear one. When the columns of the matrix are arranged to follow the cross-range path the data are not evenly sampled across the ROI. To mitigate this separation, the reconstruction algorithm uses interpolation after the mapping to obtain even sampling. Figure 4-6 shows the mapping, and how the distance between the points in the cross-range position is increased as the distance from the center of the scan geometry, increases.

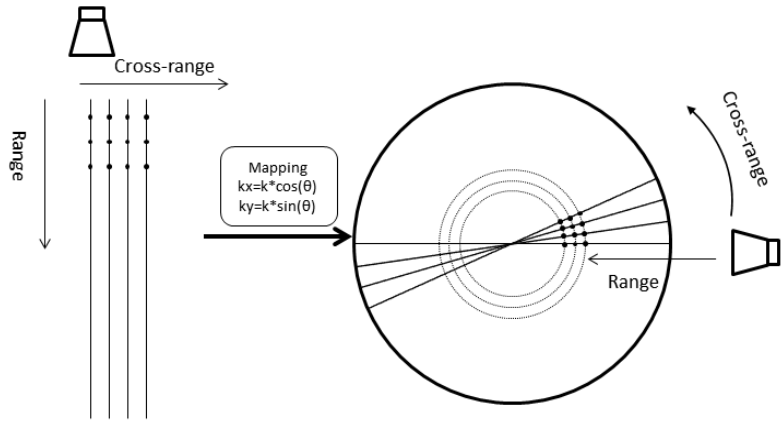

Figure 4-6 Mapping done during the holographic reconstruction. On the left, the raw data matrix is shown, where the rows are the cross-range and columns the range domain. On the right, the mapping arranges the columns to follow the cross-range path of the scan geometry. As we move away from the center of the scan geometry, the sample points separation is increased in the cross-range direction.

Due to the scan trajectory and the mapping, there is an oversampling at the center of the image when it is reconstructed. This means that if a homogenous image is reconstructed by this algorithm, an artifact at the center of the ROI is shown. This phenomenon is illustrated in Figure 4-7.

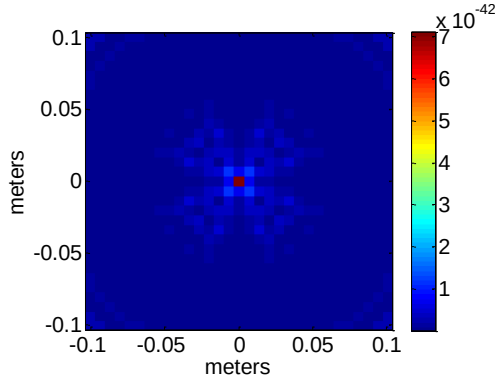

Figure 4-7 Reconstructed image of a homogeneous input. Due to the nature the reconstruction algorithm, an artifact is formed at the center of the image.

Figure 4-1 shows that if the speed of the wave is overestimated the targets shift to the center of the image. This behavior is aggravated by the artifact found at the center of the image. When the IQM were used, the presence of the artifact at the center impairs the ability to estimate the propagation speed correctly.

Different approaches were used to compensate for the artifact. The first method employed a filter in the frequency domain. Next, compensation based on the oversampling at the center was tried. Finally, a simple inverted top hat function in the time domain was implemented.

The problem shown in Figure 4-6 is also shared by CT scans. A common technique to compensate for such an artifact is to use a ramp filter in the frequency domain. To avoid amplification of the noise, the ramp filter is cut-off before the high frequencies are reached. An alternative approach to diminish noise is to taper the ramp filter using a sinc function. [45]

$$Q(\omega) = \begin{cases} \pi * \omega & \omega \leq \omega_{lim} \\ 0 & \omega > \omega_{lim} \end{cases} \tag{4.5}$$

$$Q_{sl}(\omega) = Q(\omega) * sinc\left(\frac{\omega}{2*\omega_{max}}\right) \quad (4.6)$$

Equations 4.5 and 4.6 show the filter used in CT scan. $Q(\omega)$ is a simple ramp filter limited to $\omega_{\lim}$ and $Q_{sl}(\omega)$ is a tapered ramp filter. Using this filter does diminish the presence of the artifact in the center of the image but not sufficiently. In a CT scan, x-rays are used, and these rays follow a more controlled path than the signal generated by an antenna.

A more complex function was generated by measuring how the algorithm changes the intensity of different targets at different positions from the center of the scan geometry. The result of this measurement is shown in Figure 4-8. This function eliminated the artifact at the center. The reason this function was not used is that it would widen the PSF of targets far from the center of the image.

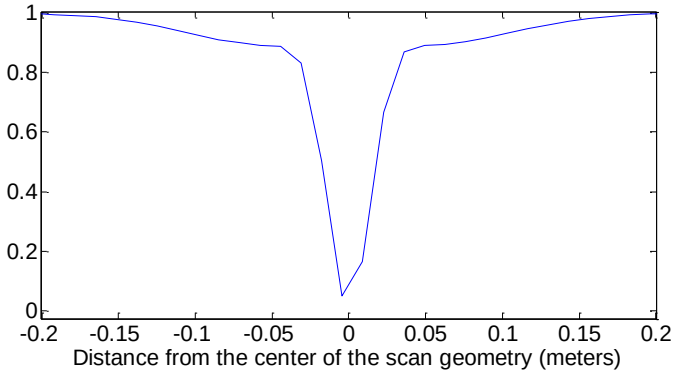

Figure 4-8 Function used to compensate for the artifact formed in the center of the image. This function was generated by measuring the intensity of a target that is shifted from the center of the ROI to the edge of it.

Finally, a simpler solution was tried. Based on the previous function a simple inverted hat function was used to diminish the response from the center of the image (Figure 4-9). This function reduces the artifact at the center in a satisfactory manner and does not changes other characteristics of the image.

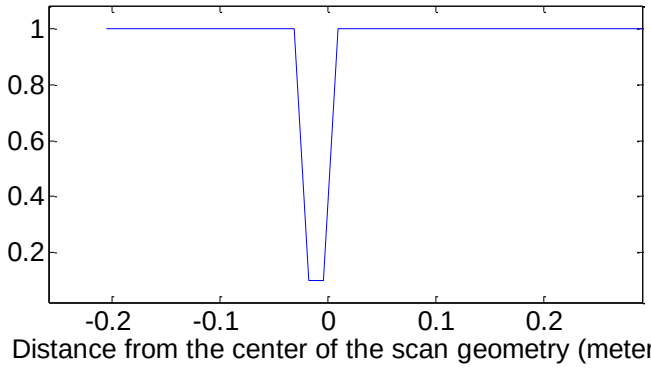

Figure 4-9 simple inverted top hat function used to compensate for the artifact formed in the center of the image. This function is based on the function shown in Figure 4-8

4.6 Results of IQM in experimental phantoms.

For the experimental results, the number of IQM was expanded to include, maximum value, Laplace, entropy, variance, Tenengrad, and contrast.

The first sets of phantoms used to test the IQM are the ones presented in Chapter 2, Figure 2-17. For this experiment, the custom horn antenna was used in air, with a glycerin phantom. To calculate the speed used in reconstruction, we average the speed of the wave in air and glycerin and weight it by the percentage of the distance the speed travels in each medium. Following this, an estimated speed of 2.4 $x10^8$ m/s was calculated. We compare the result of the IQM to this speed.

In this first set of experiments the maximum value, the variance, and Tenengrad all yield a speed that is within 10% of the calculated speed of $2.4x10^8$ m/s. Table 4-4 shows the summary of the results obtained. The results demonstrate that Tenengrad has, on average, the closest speed to $2.4x10^8$ m/s.

Type	Maximum	Laplace	Entropy	Variance	Tenengrad	contrast
No Tumor	2.59E+08	2.59E+08	2.59E+08	2.59E+08	2.59E+08	2.59E+08
Tumor at R	2.30E+08	2.54E+08	2.59E+08	2.36E+08	2.36E+08	2.54E+08
Tumor at D	2.59E+08	2.59E+08	2.89E+08	2.59E+08	2.59E+08	2.59E+08
Tumor at L	2.44E+08	2.83E+08	2.91E+08	2.46E+08	2.36E+08	2.89E+08
Tumor at U	2.57E+08	2.59E+08	2.89E+08	2.59E+08	2.59E+08	2.89E+08

Table 4-4 Speeds calculated by the IQM for the horn antenna in air. In the blue background are the speeds that are within 5% of the target speed, a white background marks the speeds within 10%, while gray background shows the speeds that are too far from the target speed to be useful. All the speeds are in m/s. NT=no tumor, TR = Tumor at R position (closest to antenna), TD= tumor at D position (side of fibroglandular patch), TL= tumor at L position (behind fibroglandular target), TU = tumor at U position (side of fibroglandular patch)

To measure how much the speed change affects the image quality we measure the SNR, SCR, TFR, and the maximum position error. This is done for the speed of $2.3x10^8$, $2.4x10^8$, $2.6x10^8$ m/s. Table 4-5 shows the results of the quality of the image. The metrics show that there is no significant difference in the quality when the speed is within 10% of the target speed. The SNR is the same across the three images when accounting for uncertainties. While the TFR may be different in four cases, the TFR is a little bit higher in the speeds selected by the IQM. There is no case where the TFR falls from 5. The worst comparison occurs in the SCR when contrasting $2.4x10^8$ with $2.6x10^8$ m/s. This is reflected in Figure 4-10 where the magnitude of clutter is higher for the image using $2.6x10^8$ m/s. Despite these differences, all three images show the targets close to the same position, and in all images, there is a contrast between healthy and malignant tissue.

Speed of $2.4x10^8$ m/s (target speed)				
Type	SNR (dB) (±1.2)	SCR (dB) (±0.4)	TFR (dB) (±0.4)	Error (m.) (± 0.004 m)
NT	18.5	5.3	NA	0.040
TR	22.5	13.1	24.7	0.038
TD	19.1	10.0	15.2	0.043
TL	16.2	5.7	8.3	0.068
TU	18.8	10.2	18.6	0.048

Speed of $2.3x10^8$ m/s				
Type	SNR (dB) (±1.2)	SCR (dB) (±0.4)	TFR (dB) (±0.4)	Error (m.) (± 0.004 m)
NT	17.4	5.0	NA	0.045
TR	22.4	14.1	26.2	0.037
TD	18.1	10.3	17.2	0.046
TL	14.9	6.2	8.1	0.075
TU	17.8	10.1	17.6	0.062

Speed of $2.6x10^8$ m/s				
Steps	SNR (dB) (±1.2)	SCR (dB) (±0.4)	TFR (dB) (±0.4)	Error (m.) (± 0.004 m)
NT	17.9	5.1	NA	0.030
TR	21.7	13.4	22.2	0.028
TD	18.4	8.4	17.7	0.026
TL	14.9	2.7	7.9	0.038
TU	18.4	8.2	17.5	0.016

Table 4-5 illustrates the analysis of the reconstructed images using different speeds. A gray background indicates that the difference of the metric, when compared to the target metric, is higher than the error value. Most of the metrics show that within the range of $2.3x10^8$ to $2.6x10^8$ m/s the SNR of the image is similar. NT=no tumor, TR = Tumor at R position (closest to antenna), TD= tumor at D position (side of fibroglandular patch), TL= tumor at L position (behind fibroglandular target), TU = tumor at U position (side of fibroglandular patch)

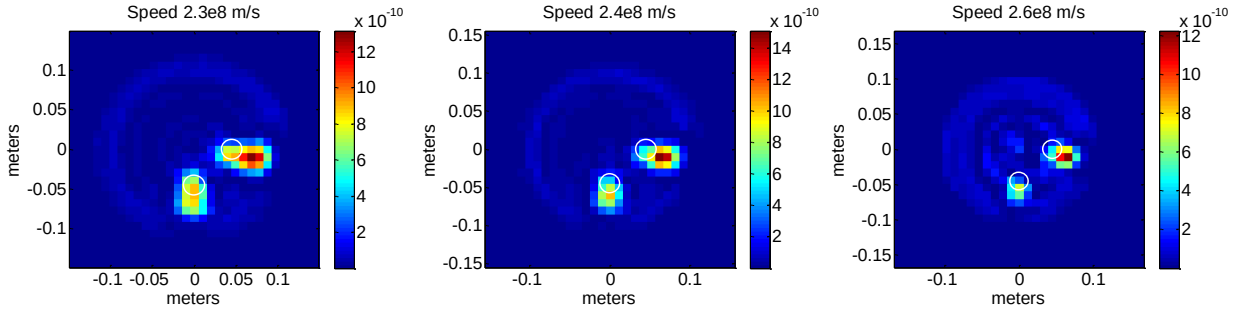

Figure 4-10 Datasets without tumor reconstructed at different speeds.

The IQM were also tested using the phantoms capture using oil as a coupling medium. Table 4-6 contains the results of the IQM. For this case, only the Tenengrad metric got a speed within 10% for all datasets.

Type	Maximum	Laplace	Entropy	Variance	Tenengrad	contrast
No Tumor	1.58E+08	2.17E+08	1.69E+08	1.58E+08	1.58E+08	1.58E+08
Tumor at R	2.17E+08	2.17E+08	2.17E+08	2.17E+08	1.58E+08	1.96E+08
Tumor at D	1.69E+08	1.66E+08	1.69E+08	1.58E+08	1.58E+08	1.58E+08
Tumor at L	1.64E+08	1.58E+08	1.64E+08	1.58E+08	1.58E+08	1.58E+08
Tumor at U	1.82E+08	1.82E+08	1.82E+08	1.69E+08	1.69E+08	1.69E+08

Table 4-6 Speeds calculated by the IQM for the horn antenna in air. White background marks the speeds within 10%, while gray background shows the speeds that are too far from the target speed to be useful. All the speeds are in m/s. NT=no tumor, TR = Tumor at R position (closest to antenna), TD= tumor at D position (side of fibroglandular patch), TL= tumor at L position (behind fibroglandular target), TU = tumor at U position (side of fibroglandular patch)

A new set of data sets were recorded to test the IQM. This set was recorded using the bed system and new antenna. The phantom was filled with glycerin and a mixture of glycerin and water. Since this mixture has a higher permittivity, there is a higher attenuation of the wave. To be able to record the target a highly reflective target made of metal was used. This target was moved from the edge of the phantom to the center of the phantom in increments of 0.5 cm.

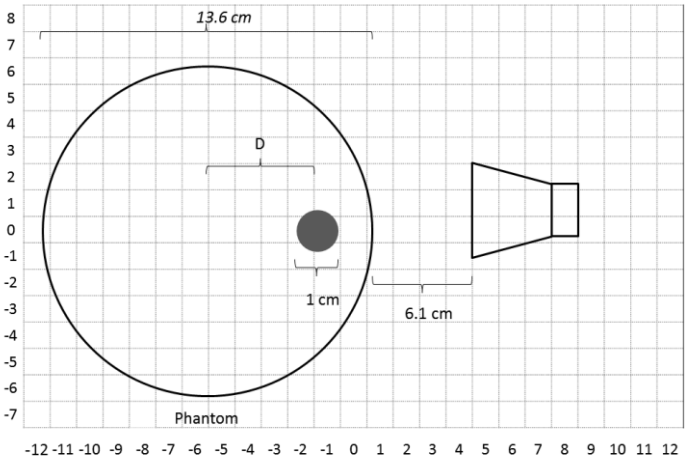

Figure 4-11 New set up to test IQM. The distance D is changed from 6.8 cm to 2.3 cm in 0.5 cm increments. The horn antenna is in air, while the phantom filling is glycerin and then modified for a mixture of water and glycerin.

For the first set, the filling of the phantom was glycerin. In this case, the target speed was 2.55×10^8 m/s, and Table 4-7 shows the results. The second set of datasets had a phantom of 90% glycerin and 10% water, with a target speed of 2.52×10^8 m/s. Table 4-8 shows the results. The last set consisted of a phantom of 80% glycerin and 20% water with a target speed of 2.48×10^8 m/s. The results are shown in Table 4-9.

Target position (cm)	Maximum	Laplace	Entropy	Variance	Tenengrad	contrast
6.8	$2.66x10^8$	$2.76x10^8$	$2.07x10^8$	$2.73x10^8$	$2.73x10^8$	$2.10x10^8$
6.3	$2.71x10^8$	$2.71x10^8$	$1.92x10^8$	$2.71x10^8$	$2.71x10^8$	$1.95x10^8$
5.8	$2.63x10^8$	$2.68x10^8$	$2.02x10^8$	$2.68x10^8$	$2.66x10^8$	$2.02x10^8$
5.3	$2.68x10^8$	$2.68x10^8$	$2.68x10^8$	$2.68x10^8$	$2.68x10^8$	$1.92x10^8$
4.8	$2.66x10^8$	$2.68x10^8$	$1.92x10^8$	$2.68x10^8$	$2.68x10^8$	$1.92x10^8$
4.3	$2.51x10^8$	$3.10x10^8$	$1.92x10^8$	$3.10x10^8$	$2.51x10^8$	$3.10x10^8$
3.8	$2.51x10^8$	$3.10x10^8$	$2.51x10^8$	$2.51x10^8$	$2.51x10^8$	$3.10x10^8$
3.3	$2.51x10^8$	$3.10x10^8$	$2.51x10^8$	$2.51x10^8$	$2.51x10^8$	$3.10x10^8$
2.8	$2.68x10^8$	$3.10x10^8$	$3.10x10^8$	$2.68x10^8$	$2.68x10^8$	$3.10x10^8$
2.3	$2.68x10^8$	$2.68x10^8$	$3.10x10^8$	$2.68x10^8$	$2.68x10^8$	$3.10x10^8$

Table 4-7 Speeds calculated by the IQM for the horn antenna in air and glycerin phantom. A single target that is shifted from 6.8 cm to 2.3 cm in 0.5 increments was used. White background marks the speeds within 10%, while gray background shows the speeds that are too far from the target speed to be useful.

Target position (cm)	Maximum	Laplace	Entropy	Variance	Tenengrad	contrast
6.8	$2.72x10^8$	$2.82x10^8$	$2.90x10^8$	$2.78x10^8$	$2.78x10^8$	$1.86x10^8$
6.3	$2.84x10^8$	$2.84x10^8$	$2.90x10^8$	$2.80x10^8$	$2.80x10^8$	$1.91x10^8$
5.8	$2.76x10^8$	$2.67x10^8$	$2.51x10^8$	$2.69x10^8$	$2.69x10^8$	$1.76x10^8$
5.3	$2.82x10^8$	$2.63x10^8$	$2.74x10^8$	$2.69x10^8$	$2.59x10^8$	$1.76x10^8$
4.8	$2.63x10^8$	$2.51x10^8$	$2.63x10^8$	$2.49x10^8$	$2.47x10^8$	$2.43x10^8$
4.3	$2.49x10^8$	$2.51x10^8$	$2.53x10^8$	$2.49x10^8$	$2.49x10^8$	$2.43x10^8$
3.8	$2.51x10^8$	$2.51x10^8$	$2.59x10^8$	$2.51x10^8$	$2.51x10^8$	$2.51x10^8$
3.3	$2.51x10^8$	$2.47x10^8$	$2.51x10^8$	$2.51x10^8$	$2.35x10^8$	$2.51x10^8$
2.8	$2.23x10^8$	$2.21x10^8$	$2.23x10^8$	$2.21x10^8$	$2.21x10^8$	$2.76x10^8$
2.3	$2.23x10^8$	$2.23x10^8$	$2.23x10^8$	$2.23x10^8$	$2.23x10^8$	$2.53x10^8$

Table 4-8 Speeds calculated by the IQM for the horn antenna in air and a 90 % glycerin-10% water phantom. A single target that is shifted from 6.8 cm to 2.3 cm in 0.5 increments is used. White background marks the speeds within 10%, while gray background shows the speeds that are too far from the target speed to be useful.

Target position (cm)	Maximum	Laplace	Entropy	Variance	Tenengrad	contrast
6.8	$2.80x10^8$	$2.82x10^8$	$2.61x10^8$	$2.78x10^8$	$2.76x10^8$	$1.86x10^8$
6.3	$2.80x10^8$	$2.82x10^8$	$2.90x10^8$	$2.67x10^8$	$2.69x10^8$	$3.10x10^8$
5.8	$2.67x10^8$	$2.67x10^8$	$2.90x10^8$	$2.69x10^8$	$2.61x10^8$	$2.80x10^8$
5.3	$2.59x10^8$	$2.67x10^8$	$2.90x10^8$	$2.69x10^8$	$2.69x10^8$	$1.78x10^8$
4.8	$2.55x10^8$	$2.47x10^8$	$2.55x10^8$	$2.53x10^8$	$2.43x10^8$	$2.35x10^8$
4.3	$2.45x10^8$	$2.49x10^8$	$3.10x10^8$	$2.45x10^8$	$2.47x10^8$	$2.51x10^8$
3.8	$2.90x10^8$	$2.90x10^8$	$2.90x10^8$	$2.90x10^8$	$2.90x10^8$	$2.35x10^8$

Table 4-9 Speeds calculated by the IQM for the horn antenna in air and an 80 % glycerin-20% water phantom. A single target that is shifted from 6.8 cm to 3.8 cm in 0.5 cm increments is used. White background marks the speeds within 10%, while gray background shows the speeds that are too far from the target speed to be useful. After 3.8 cm the attenuation from the phantom was too high to have any reflection from the target.

The purpose of moving the same target in 0.5 intervals was to confirm that the IQM are focusing on an average speed of the full scan geometry, instead of the speed that only favors one of the targets. Table 4-7 shows that Tenengrad was within 10% of the target speed, irrespective of the target position.

The objective of changing the dielectric properties of the phantom was to test the IQM at different speeds. However, due to attenuation for high dielectric property materials, the experiment was only possible with three different phantom fillings. Unfortunately, the three fillings that were tested were within 10% of each other, so the metrics could not discriminate between them.

4.7 Conclusion

Overall the metric that performed the best was Tenengrad, with the maximum of the image being a close second. The results demonstrate that if the IQM produce a result that is within 10% of the target speed the image retains the characteristics of an image reconstructed using the target speed.

Future work should include testing the IQM using complex phantoms that mimic the structure of real breast, instead of point-like structures. It is also desirable to resolve the artifact problem described in Section 4.4 with a more elegant solution since the inverted top hat function used may not work well for targets that are close to the center.

5 Conclusions and Recommendations

BMI is a growing field that has a promising future as an aid for breast cancer detection. The present thesis aims to lay the groundwork for future BMI systems that will be used in clinical trials. To be able to accurately reconstruct the position of the tumor with minimal artifacts the wave propagation speed in the medium must be known. To achieve this goal, experimental datasets collected with matching media consisting of oil and air were generated and then used to test algorithmic approaches that use different image quality metrics to determine the propagation speed.

Chapter 2 presents a characterization of hardware for breast microwave radar systems using three different antennas, and two different coupling media is presented. The chapter describes the strengths and compromises of various design decisions for a BMI system. A broadband antenna is desired with an H-plane beamwidth that covers the ROI and an E-plane pattern that is as narrow as possible to allow for scans in different coronal slices. The antenna has to be paired with a VNA that can match the properties of the antenna, especially the bandwidth. A high output power and fast scan time allow for a robust system.

The use of a coupling medium that is well matched to the breast tissue may offer advantages, such as a lower diffraction at the interface and as a natural shield from external noise. However, if the attenuation of the coupling medium increases, a more sensitive VNA is needed. In this work, the image quality obtained when canola oil was used as a coupling medium was compared to that when the imaging was performed in air. While the noise was similar (±2 dB difference in SNR) when using air or oil as a matching medium, the contrast between tumor and fibroglandular tissue was better when air was used.

Future work should include the design of an antenna that would better match the required specifications, and which could be reliably manufactured.

Chapter 3 presents a mathematical theory for identifying the minimum number of scan locations, and a test of this theory using experimental results. Knowing the number of scan locations that are required allows for a better understanding of the compromise between the volume of data that needs to be collected and the time taken to complete a scan. The results presented in this work showed that for an antenna in air, there is no increase in image quality for more than 36 scan locations. While this is a reasonable guide to the optimal number of scan locations, future work is required to confirm whether this is still true with more complex phantoms and in patients.

Chapter 4 describes a novel speed-search algorithm that uses image quality metrics as criteria for determining the propagation speed. The Tenengrad algorithm was the most reliable and was capable of finding speeds within 10% of the target speed for phantoms using point-like targets. Image quality was found to vary slowly with propagation speed and did not change significantly within this 10% range. Future work should focus on using a more complex search method instead of a linear search, and testing the algorithm using complex phantoms that better mimic the breast.

The results presented in this work are promising. There is ongoing work to build complex phantoms that mirror a breast, and the current work offers a starting point for testing these complex phantoms and for using the system for clinical trials. The antenna characterisation opens design options that allow for a system focused on imaging women. The study on sampling constraints weights the need for a fast scan against the need for information to obtain useful data. The novel speed search algorithm allows for the scan of unknown phantoms or human subjects that may have

a diverse array of dielectric properties. These three main topics of this work allow for improvements needed to evolve the BMI system used in the lab to a system that can be used for clinical trials.

References

[1] Canadian Cancer Society's Steering Committee, Canadian Cancer Statistics 2015. Canadian Cancer Society, Toronto, Canada, 2015.

[2] Sree, Subbhuraam Vinitha, et al. "Breast imaging: A survey." World journal of clinical oncology 2.4 (2011): 171.

[3] Lee, Carol H., D. David Dershaw, Daniel Kopans, Phil Evans, Barbara Monsees, Debra Monticciolo, R. James Brenner et al. "Breast cancer screening with imaging: recommendations from the Society of Breast Imaging and the ACR on the use of mammography, breast MRI, breast ultrasound, and other technologies for the detection of clinically occult breast cancer." Journal of the American College of Radiology vol. 7, no. 1, 2010, pp.18-27.

[4] Hiebel, Michael. Fundamentals of vector network analysis. Rohde & Schwarz, 2007.

[5] Balanis, Constantine A. Antenna theory: analysis and design. John Wiley & Sons, 2012.

[6] Richards MA. Fundamentals of radar signal processing. Tata McGraw-Hill Education; 2005 Oct 1.

[7] Nikolova N. Microwave imaging for breast cancer. IEEE Microwave Magazine. 2011;7(12):78-94.

[8] Vander Vorst A, Rosen A, Kotsuka Y. RF/microwave interaction with biological tissues. John Wiley & Sons; 2006 Feb 6.

[9] Mohammed BJ, Abbosh AM, Mustafa S, Ireland D. Microwave system for head imaging. Instrumentation and Measurement, IEEE Transactions on. 2014 Jan;63(1):117-23.

[10] O'Halloran M, Morgan F, Flores-Tapia D, Byrne D, Glavin M, Jones E. Prototype Ultra Wideband Radar System for Bladder Monitoring Applications. Progress In Electromagnetics Research C. 2012;33:17-28.

[11] Sugitani T, Kubota SI, Kuroki SI, Sogo K, Arihiro K, Okada M, Kadoya T, Hide M, Oda M, Kikkawa T. Complex permittivities of breast tumor tissues obtained from cancer surgeries. Applied Physics Letters. 2014 Jun 23;104(25):253702.

[12] Lin JC. Frequency optimization for microwave imaging of biological tissues. Proceedings of the IEEE. 1985 Feb;73(2):374-5.

[13] Epstein, N.R., Meaney, P.M. and Paulsen, K.D., 2014. 3D parallel-detection microwave tomography for clinical breast imaging. Review of Scientific Instruments, 85(12), p.124704.

[14] Li, D., Meaney, P.M., Raynolds, T., Pendergrass, S.A., Fanning, M.W. and Paulsen, K.D., 2004. Parallel-detection microwave spectroscopy system for breast imaging. Review of Scientific Instruments, 75(7), pp.2305-2313.

[15] Fang, Q., Meaney, P.M. and Paulsen, K.D., 2010. Viable three-dimensional medical microwave tomography: Theory and numerical experiments. Antennas and Propagation, IEEE Transactions on, 58(2), pp.449-458.

[16] Fear, E.C., Bourqui, J., Curtis, C., Mew, D., Docktor, B. and Romano, C., 2013. Microwave breast imaging with a monostatic radar-based system: A study of application to patients. IEEE transactions on microwave theory and techniques, 61(5), pp.2119-2128.

[17] Fear, E.C., Li, x., Hagness, S.C. and Stuchly, M.A., 2002. Confocal microwave imaging for breast cancer detection: Localization of tumors in three dimensions. Biomedical Engineering, IEEE Transactions on, 49(8), pp.812-822.

[18] Bourqui, J., Sill, J.M. and Fear, E.C., 2012. A prototype system for measuring microwave frequency reflections from the breast. Journal of Biomedical Imaging, 2012, p.9.

[19] Klemm, M., Craddock, I.J., Leendertz, J.A., Preece, A. and Benjamin, R., 2009. Radar-based breast cancer detection using a hemispherical antenna array—experimental results. Antennas and Propagation, IEEE Transactions on, 57(6), pp.1692-1704.

[20] Flores-Tapia, D. and Pistorius, S., 2011. Real time breast microwave radar image reconstruction using circular holography: A study of experimental feasibility. Medical Physics, 38(10), pp.5420-5431.

[21] Flores-Tapia, D., Thomas, G. and Pistorius, S., 2010. Wavefront reconstruction method for subsurface radar imagery acquired along circular and planar scan trajectories. Aerospace and Electronic Systems, IEEE Transactions on, 46(3), pp.1346-1363.

[22] Ostadrahimi, M., Noghanian, S., Shafai, L., Zakaria, A., Kaye, C. and LoVetri, J., 2010. Investigating a double layer Vivaldi antenna design for fixed array field measurement. International Journal of Ultra Wideband Communications and Systems, 1(4), pp.282-290.

[23] Latif, S., Pistorius, S. and Shafai, L., 2013, December. A double-ridged horn antenna design in canola oil for medical imaging. In Advances in Electrical Engineering (ICAEE), 2013 International Conference on (pp. 421-424). IEEE.

[24] Latif, S., Flores-Tapia, D., Pistorius, S. and Shafai, L., 2014. A planar ultrawideband elliptical monopole antenna with reflector for breast microwave imaging. Microwave and Optical Technology Letters, 56(4), pp.808-813.

[25] A-info, 2013, LB-20200 2-20Ghz Broadband Horn Antenna. Available from: http://www.ainfoinc.com/en/pro_pdf/new_products/antenna/Broadband%20Horn%20Antenna/tr_LB-20200.pdf . [5 April 2016].

[26] Sill, J.M. and Fear, E.C., 2005. Tissue sensing adaptive radar for breast cancer detection-experimental investigation of simple tumor models. Microwave Theory and Techniques, IEEE Transactions on, 53(11), pp.3312-3319.

[27] Solis Nepote, M., Rodriguez Herrera, D., Tapia, D.F., Latif, S. and Pistorius, S., 2014, April. A comparison study between horn and Vivaldi antennas for 1.5–6 GHz breast microwave radar imaging. In Antennas and Propagation (EuCAP), 2014 8th European Conference on (pp. 59-62). IEEE.

[28] Tapia, D.F., Rodriguez Herrera, D., Solis Nepote, M., Maizlish, A., Alabaster, C.M. and Pistorius, S., 2013, September. Holographic reconstruction of multistatic breast microwave radar images: initial results on synthetic phantoms. In *Electromagnetics in Advanced Applications (ICEAA), 2013 International Conference on* (pp. 1103-1106). IEEE.

[29] Soumekh, M., 1999. Synthetic aperture radar signal processing (pp. 5-16). New York: Wiley.

[30] Flores-Tapia, D., Maizlish, O., Alabaster, C. and Pistorius, S., 2012, May. Microwave radar imaging of inhomogeneous breast phantoms using circular holography. In Biomedical Imaging (ISBI), 2012 9th IEEE International Symposium on (pp. 86-89). IEEE.

[31] Ehrlich, P. and De, J., 1953. Dielectric Relaxation in a Styrene-Acrylonitrile Co-polymer During and After its Polymerization. Journal of Research of the National Bureau of Standards, 51(3).

[32] Golio, M. and Golio, J. eds., 2007. RF and microwave circuits, measurements, and modeling. CRC Press.

[33] Flores-Tapia, D. and Pistorius, S., 2011, March. Spatial sampling constraints on breast microwave radar scan acquired along circular scan geometries. In Biomedical Imaging: From Nano to Macro, 2011 IEEE International Symposium on (pp. 496-499). IEEE.

[34] Flores-Tapia, D., Thomas, G. and Pistorius, S., 2005, October. Effects on the Quality of Breast Microwave Imagery Using Different Antenna Beamwidths. In Applied Electromagnetics and Communications, 2005. ICECom 2005. 18t h International Conference on (pp. 1-4). IEEE.

[35] Benjamin, R., 1996, October. Synthetic, post-reception focusing in near-field radar. In The Detection of Abandoned Land Mines: A Humanitarian Imperative Seeking a Technical Solution, EUREL International Conference on (Conf. Publ. No. 431) (pp. 133-137). IET.

[36] Sjanic, Z. and Gustafsson, F., 2010, July. Simultaneous navigation and SAR auto-focusing. In Information Fusion (FUSION), 2010 13th Conference on (pp. 1-7). IEEE.

[37] Liu, L., Bai, x., Zhao, J. and Tao, R., 2010, September. SAR Autofocus Using Wiener Deconvolution. In Pervasive Computing Signal Processing and Applications (PCSPA), 2010 First International Conference on (pp. 1256-1259). IEEE.

[38] Chern, N.N.K., Neow, P.A. and Ang Jr, M.H., 2001. Practical issues in pixel-based autofocusing for machine vision. In Robotics and Automation, 2001. Proceedings 2001 ICRA. IEEE International Conference on (Vol. 3, pp. 2791-2796). IEEE.

[39] Liu, W., Shen, J. and Tan, B., 2009, October. Autofocusing Image System of CD-SEM. In Image and Signal Processing, 2009. CISP'09. 2nd International Congress on (pp. 1-3). IEEE.

[40] Wang, J. and Liu, x., 2006. SAR minimum-entropy autofocus using an adaptive-order polynomial model. Geoscience and Remote Sensing Letters, IEEE, 3(4), pp.512-516.

[41] Fortune, S.A., Hayes, M.P. and Gough, P.T., 2001. Statistical autofocus of synthetic aperture sonar images using image contrast optimisation. In OCEANS, 2001. MTS/IEEE Conference and Exhibition (Vol. 1, pp. 163-169). IEEE.

[42] Flores-Tapia, D., Thomas, G., Sabouni, A., Noghanian, S. and Pistorius, S., 2006, August. Breast tumor microwave simulator based on a radar signal model. In Signal Processing and Information Technology, 2006 IEEE International Symposium on (pp. 17-22). IEEE.

[43] Rodriguez-Herrera, D., Flores-Tapia, D. and Pistorius, S., 2014, April. Comparison of image quality metrics for electromagnetic wave propagation speed estimation in Breast Microwave Radar imaging scenarios. In Antennas and Propagation (EuCAP), 2014 8th European Conference on (pp. 516-519). IEEE.

[44] Meaney, P.M., Pendergrass, S.A., Fanning, M.W. and Paulsen, K.D., 2003. Importance of using a reduced contrast coupling medium in 2D microwave breast imaging. Journal of Electromagnetic Waves and Applications, 17(2), pp.333-355.

[45] Barrett, H.H. and Swindell, W., 1996. Radiological imaging: the theory of image formation, detection, and processing. Academic Press.